Chapter 6

WAVE PROPAGATION ALGORITHMS ON CURVED MANIFOLDS

In the remaining chapters of this thesis the details for a class of wave propagation algorithms that generate stable, accurate, and high-resolution numerical solutions to hyperbolic conservation laws on smooth manifolds are presented. Much of what has been discussed in Chapters 1 through 5 has been for the purpose of developing and implementing this algorithm. Details of the algorithm together with computational examples are presented in this chapter. An implementation of the algorithm in the software package CLAWMAN is presented in Chapter 7. Finally, in Chapter 8 the algorithm is applied to various standard test problems in relativistic hydrodynamics.

In the previous chapter, equations (5.83) and (5.87) were derived and represent, respectively, scalar and vector conservation laws in a coordinate system that covers a subset $\mathscr{U}$ of a manifold $\mathscr{M}$. We found that the flux functions in both equations gain an explicit spatial dependence through the determinant of the metric tensor. We also found that vector conservation laws are written in *weak* conservation form due to the source term generated by the representation of the divergence of a second rank tensor in the coordinate basis. Systems of conservation laws involving both scalar and vector equations were found to be expressed as a system (5.92). If the metric tensor is that of flat Euclidean space, $[h_{ij}] = \mathrm{diag}(1, 1, 1)$ in $\mathbb{R}^3$, however, then $\sqrt{h} = 1$ and $\boldsymbol{\psi} = 0$ in that equation. In that case, system (5.92) would be in a standard form handled by most high-resolution finite volume methods. It is really the spatially-varying flux and the geometrically induced source term that prevent conservation laws on manifolds from being standard problems. The main novel features of the algorithm developed in this thesis are the following:

1. Spatially-varying flux functions arising from the geometry are handled using f-waves.
2. The geometrically induced source terms for vector laws are handled using parallel transport of vector components.

In the following sections these features of the algorithm are described in detail.

The functional form of the components of equation (5.92) is a result of the choice of both state variables $\boldsymbol{q} = (q^1, \cdots, q^{n_{eq}})^T$ and the particular coordinate basis in which the conservation laws are expressed. For example, instead of choosing the tangent components of momentum ρu^i in (5.89), the cotangent components ρu_i could have been chosen and would have lead to a different functional form of the components for both the flux and source term. Similarly, a change of coordinates would lead to different components. One way to handle the terms in system (5.92) induced by the geometry of $\mathscr{M}$ is to change the basis in which the equations are expressed in order to cast them in a form that reduces, or entirely eliminates, the source terms. For example, in [78] the classical Euler equations are written in *strong conservation* form (i.e. with no source terms) by expanding a curvilinear set of basis vectors into a Cartesian basis, thereby eliminating undifferentiated terms such as Christoffel symbols. The resulting system consists of a hybrid set of equations containing both Cartesian and curvilinear elements. On a manifold, however, a single Cartesian basis does not exist. In [65], symmetry of the manifold is used to generate a basis that reduces the number of components in the source $\boldsymbol{\psi}$. The reduction of the number of components in the source is dependent on both the system of conservation laws and the geometry of the manifold on which this system is to be solved. The algorithm described here does not attempt to recast the equations or to eliminate the source terms that appear for conservation laws on manifolds. Rather, the algorithm handles them the way they appear in system (5.92).

Various methods have been developed to handle systems of balance laws in the form (5.92). One simple approach that is often used is based on fractional time steps. This method generates the solution by alternating between solving the homogeneous version of the system (5.92) and the ordinary differential equations

$$\boldsymbol{q}_{,t} = \boldsymbol{\psi}(\boldsymbol{q}, \vec{x}). \tag{6.1}$$

An example of such an *operator-split* method is developed in [20] and applied to the system of equations describing relativistic test fluids. Another approach is to use a *method of lines* discretization as in [21] and [67]. In this method the geometrically induced source term appears on the right hand side of the resulting system of ordinary differential equations (ODEs). A time-stepping algorithm that preserves the conservative properties of numerical flux functions computed at cell interfaces can then be applied to the system of ODEs.

The algorithms developed in this chapter share many features with the methods developed in [6] and [20]. Each of these methods, like the algorithms developed here, is based on the solution of Riemann problems and make use of limiters near discontinuities to generate non-oscillatory solutions. However, the basic cell updates, methods used to achieve spatial accuracy, and the way source terms are handled are different. Cell updates and spatial accuracy are generated using f-waves first discussed in Section 3.1, and applied to curved manifolds in Section 6.4. Source terms are handled *locally* by discrete parallel propagation operators that act on vector components of $\boldsymbol{q}$ and $\boldsymbol{f}$ as described in Section 6.5.

6.1 The coordinate grid

The algorithm presented in this chapter is implemented on a logically rectangular finite volume grid that covers a subset $\mathscr{U}$ of a smooth manifold $\mathscr{M}$. It is not necessary that a single coordinate system entirely cover $\mathscr{U}$. It may be convenient, as we saw in Figure 1.1, to cover $\mathscr{U}$ with multiple coordinate systems. In fact, the only requirement for the grid in the algorithm presented here is that the metric tensor remain smooth in each grid cell. This means that two adjacent cells can be described by two entirely different coordinate systems as long as within each cell the coordinate basis is smoothly varying. A jump in metric components across a cell interface can be handled by the way in which Riemann problems are solved and source terms are treated. This feature of the method is beneficial for manifolds like the sphere, $\mathcal{S}^2$, that are often covered by multiple coordinate systems.

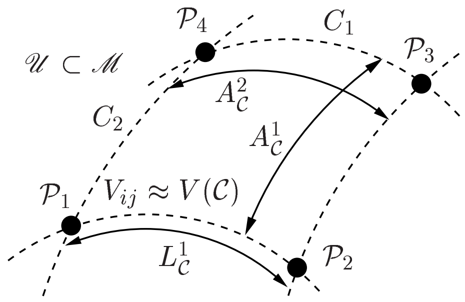

(a) Physical cell

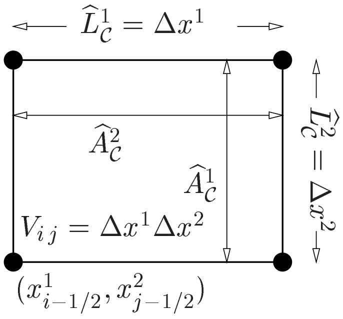

(b) Computational cell

Figure 6.1: (a) The physical cell consists of the four points $\{\mathcal{P}_1, \mathcal{P}_2, \mathcal{P}_3, \mathcal{P}_4\}$ connected by the coordinate curves C_1 and C_2 and has a volume $V(\mathcal{C}) = \int_{\mathcal{C}} \sqrt{h}\, dx^1\, dx^2$. (b) The cell as it is represented on the computational grid. The volume is approximated by $V_{ij} = \sqrt{h_{ij}}\, \Delta x^1\, \Delta x^2 \approx V(\mathcal{C})$.

LeVeque and Rossmanith [50] have used this feature to compute geophysical flows on a sphere covered by the six coordinate systems shown in Figure 1.1.

Consider a single coordinate system, $\mathscr{X}$, that covers $\mathscr{U} \subset \mathscr{M}$, has coordinate functions x^k and basis vectors $\vec{\partial}_{(k)}$ for $k \in \{1, \cdots, n_d\}$. Both the examples and figures used here are two dimensional so that $n_d = 2$, but the geometric description is kept general for the extension of the algorithm to higher spatial dimensions. The coordinate region is discretized into a grid of logically rectangular finite volume cells

$$\begin{aligned} \mathcal{C}_{ij} &= \left(x^1_i - \Delta x^1/2, x^1_i + \Delta x^1/2\right) \times \left(x^2_j - \Delta x^2/2, x^2_j + \Delta x^2/2\right) \\ &\equiv \left(x^1_{i-1/2}, x^1_{i+1/2}\right) \times \left(x^2_{j-1/2}, x^2_{j+1/2}\right), \end{aligned} \tag{6.2}$$

with a natural extension for $\mathcal{C}_{ijk}$ in three dimensions. The numerical solution is evolved in the coordinate grid shown in Figure 6.1(b). It follows that coordinate lengths, cross-sectional areas, and volumes of this cell must be related to the corresponding physical quantities by the metric tensor. Useful coordinate quantities are depicted in Figure 6.1(b) and defined by the following:

$$\begin{aligned} \widehat{L}^k_{\mathcal{C}} &= \Delta x^k; && \text{the coordinate length of each edge in } \mathcal{C}, \\ \widehat{A}^k_{\mathcal{C}} &= \prod_{\substack{i=1 \\ i\neq k}}^{n_d} \Delta x^i; && \text{the coordinate cross-sectional area of } \mathcal{C} \text{ along } C_k, \\ \widehat{V}_{\mathcal{C}} &= \prod_{i=1}^{n_d} \Delta x^i; && \text{the coordinate volume of } \mathcal{C}. \end{aligned} \tag{6.3}$$

Often the coordinate quantities will refer to a particular cell in which case the subscript $\mathcal{C}$ is replaced by indices. For example, the coordinate lengths, cross-sectional areas, and volume in $\mathcal{C}_{ij}$ are denoted by $\widehat{L}^k_{|ij}$, $\widehat{A}^k_{|ij}$, and $\widehat{V}_{|ij}$, respectively, and the notation that subscripts following a $|$ denote cell indices. This notation will be used for quantities with which there may be confusion between subscripts that represent cell indices or cotangent components.

Each quantity listed above has a physical counterpart depicted in Figure 6.1(a). The physical and coordinate quantities are related to each other by the metric tensor. The true volume of the cell, $V(\mathcal{C})$, depicted in Figure 6.1(a), can be approximated by the physical volume $V_{\mathcal{C}}$ of the logically rectangular grid cell using the determinant of the metric tensor

$$\begin{aligned} V_{|ij} = \sqrt{h}_{|ij}\,\widehat{V}_{|ij} &= \sqrt{h}_{|ij}\,\Delta x^1\,\Delta x^2 \\ &\approx \int_{\mathcal{C}_{ij}} \sqrt{h}\,dx^1\,dx^2, \end{aligned} \tag{6.4}$$

where, once again, the notation that subscripts following a $|$ represent cell indices has been used. This notation is necessary since representing the determinant h in $\mathcal{C}_{ij}$ by h_{ij} may be confused with the cotangent components of the metric tensor $\overleftrightarrow{h}$ in the previous equation. Using subscripts that follow a $|$ to denote cell indices will eliminate any such confusion.

The physical distance traversed for a given coordinate displacement along each C_k can also be related to its coordinate counterpart, $\widehat{L}^k_{\mathcal{C}}$, using the metric. For example, the physical length of the lower edge of $\mathcal{C}_{ij}$, shown in Figure 6.1(a), is the distance along C_1 between points $\mathcal{P}_1$ and $\mathcal{P}_2$. This can be calculated using equation (5.53) together with the fact that $dx^2 = 0$ along this curve. The result is

$$\begin{aligned} L^1_{|i,j-1/2} = \sqrt{h}_{11|i,j-1/2}\,\widehat{L}^1_{|i,j-1/2} &= \sqrt{h}_{11|i,j-1/2}\,\Delta x^1 \\ &\approx |\mathcal{P}_2 - \mathcal{P}_1| \end{aligned} \tag{6.5}$$

where the notation defined above has been used so that the value of the metric component h_{ij} along the lower edge of $\mathcal{C}_{ij}$ has been denoted by $h_{ij|i,j-1/2}$. Note that the comma separating cell indices after the $|$ do not refer to partial differentiation. The physical distance along the left vertical edge between points $\mathcal{P}_1$ and $\mathcal{P}_4$ can be computed in a similar way using $\sqrt{h}_{22|i-1/2,j}$.

Finally, each physical cross section, $A^k_{\mathcal{C}}$, represents the area through which flux densities pass as material moves out of one cell and into another along x^k. They can be related to $\widehat{A}^k_{\mathcal{C}}$ by the *volume* element on the sub-manifold defined by the *coordinate plane* of the cross section. By keeping x^k fixed and allowing the other coordinates x^i, for $i \neq k$ to vary within the cell, a coordinate plane is established on which the restricted metric, $\overleftrightarrow{h}^{\perp}$, is defined. Since one of the coordinates is frozen in this sub-manifold, the volume element will have dimension $n_d - 1$. Therefore, in a three-dimensional grid, the volume elements of such sub-manifolds will be cross-sectional areas. However, in a two-dimensional grid, they represent one-dimensional lengths.

If, for example, $n_d = 2$, then there are two restricted metrics, one for each coordinate direction. The matrix representation of each restricted metric is 1×1:

$$\begin{aligned} \left[h^{\perp^1}_{ij}\right] &= h_{22}; \quad \text{along the } x^1 \text{ coordinate,} \\ \left[h^{\perp^2}_{ij}\right] &= h_{11}; \quad \text{along the } x^2 \text{ coordinate.} \end{aligned} \tag{6.6}$$

The fact that these restricted metrics only have one element is due to the fact that the coordinate planes in this case are represented by lines. We will use the name *coordinate plane* since it refers to the cross section of a cell with $n_d = 3$ which is, in fact, a plane. In three spatial dimensions the metric tensor restricted to the coordinate plane along x^1 will have the form

$$\left[h^{\perp^1}_{ij}\right] = \begin{pmatrix} h_{22} & h_{23} \\ h_{23} & h_{33} \end{pmatrix}, \tag{6.7}$$

with similar restricted metrics for the other two cross sections of the cell.

The volume element associated with $h^{\perp^k}_{ij}$ is

$$A^k_{\mathcal{C}} = \sqrt{h^{\perp^k}}\, \widehat{A}^k_{\mathcal{C}} = \sqrt{h^{\perp^k}} \prod_{\substack{i=1 \\ i \neq k}}^{n_d} \Delta x^i, \tag{6.8}$$

where $h^{\perp^k}$ is the determinant of the matrix $\left[h^{\perp^k}_{ij}\right]$. The last equation defines the physical area through which material passes when traveling in the x^k-direction. As mentioned above, if $n_d = 2$ this volume element represents a length, and if $n_d = 3$ it represents an area.

The preceding definitions of the physical quantities $V_{\mathcal{C}}$, $A^k_{\mathcal{C}}$, and $L^k_{\mathcal{C}}$ can be used to define the following important ratios for a coordinate grid cell:

$$\begin{aligned} \mathcal{V}_{\mathcal{C}} &= \frac{V_{\mathcal{C}}}{\widehat{V}_{\mathcal{C}}} = \sqrt{h_{\mathcal{C}}}; && \text{the ratio of physical to coordinate volume for the cell denoted by } \mathcal{C}, \\ \mathcal{A}^k_{\mathcal{C}} &= \frac{A^k_{\mathcal{C}}}{\widehat{A}^k_{\mathcal{C}}} = \sqrt{h^{\perp^k}}_{\mathcal{C}}; && \text{the ratio of physical to coordinate cross-sectional area along } x^k \text{ in } \mathcal{C}. \end{aligned} \tag{6.9}$$

The ratios $\mathcal{V}_{\mathcal{C}}$ and $\mathcal{A}^k_{\mathcal{C}}$ are defined as the square root of the determinant of the metric and restricted metric, respectively. Using properties of the determinant, these ratios can be related to the components of the inverse metric tensor by the relationship

$$\mathcal{A}^k = \mathcal{V}\sqrt{h^{kk}}, \tag{6.10}$$

which is true at each point in $\mathscr{U} \subset \mathscr{M}$. One can conclude from the previous equation that the physical volume on $\mathscr{M}$ is a product of A^k and a length perpendicular to the coordinate plane that defines A^k. For example, consider an orthogonal coordinate basis so that the off-diagonal elements of $[h_{ij}]$ vanish and $h^{kk} = 1/h_{kk}$. Use this in equation (6.10) and multiply through by $\widehat{V}$ to find

$$\begin{aligned} V &= A^k \sqrt{h_{kk}}\, \Delta x^k \\ &= A^k L^k_. \end{aligned} \tag{6.11}$$

For a coordinate basis that is not orthogonal, the use of the inverse metric component means that the length is defined in terms of the cotangent basis which, as we saw in Figure 5.6, measures distance perpendicular to the coordinate plane that defines A^k.

6.2 Flux differences on a manifold

The definitions of the previous section can now be used to write down a numerical method on $\mathscr{M}$ that is based on flux differences and analogous to the multidimensional version of (2.5). The method is based on integrating the conservation law (1.1) from t to $t + \Delta t$ on the coordinate basis previously described. The result is

$$\begin{aligned}\int_{\mathcal{C}} \boldsymbol{q}(t+\Delta t, x^k)\,\sqrt{h}\,d^{n_d}x = \int_{\mathcal{C}} \boldsymbol{q}(t, x^k)\,\sqrt{h}\,d^{n_d}x \\ - \int_t^{t+\Delta t} \sum_{i=1}^{n_d} \Bigg(\int_{\widehat{A}^i_{\mathcal{C}+}} \boldsymbol{f}\left(\boldsymbol{q}(t, x_{i+1/2})\right) \cdot \sqrt{h}\, \vec{dx}^{(i)} \\ + \int_{\widehat{A}^i_{\mathcal{C}-}} \boldsymbol{f}\left(\boldsymbol{q}(t, x_{i-1/2})\right) \cdot \sqrt{h}\, \vec{dx}^{(i)} \Bigg)\, dt,\end{aligned} \tag{6.12}$$

where the subscript in $\widehat{A}^i_{\mathcal{C}\pm}$ denotes that the coordinate area is measured at the left or right edge of $\mathcal{C}$ along x^i. In the previous equation $d^{n_d}x = dx^1 \times \cdots \times dx^{n_d}$, and $\vec{dx}^{(i)}$ is the surface normal vector to the coordinate plane that defines the area $\widehat{A}^i_{\mathcal{C}}$.

Finite volume averages similar to (2.1) used in the standard algorithm are defined by

$$\boldsymbol{Q}^n_{\mathcal{C}} = \frac{1}{V_{\mathcal{C}}} \int_{\mathcal{C}} \boldsymbol{q}(t^n, x^k)\,\sqrt{h}\,d^{n_d}x \approx \frac{1}{V(\mathcal{C})} \int_{\mathcal{C}} \boldsymbol{q}(t^n, x^k)\,\sqrt{h}\,d^{n_d}x, \tag{6.13}$$

where the square root of the determinant is present to account for the volume of the cell. The numerical flux defined in (2.4) is generalized for a manifold as

$$\hat{\boldsymbol{F}}^{(i)}_{\mathcal{C}} \approx \frac{1}{\Delta t} \int_t^{t+\Delta t} \left(\frac{1}{A^i_{\mathcal{C}}} \int_{\widehat{A}^i_{\mathcal{C}}} \boldsymbol{f}\left(\boldsymbol{q}(t, x^k)\right) \cdot \sqrt{h}\, \vec{dx}^{(i)} \right) dt, \tag{6.14}$$

and represents the time-averaged *flux per unit area* moving through the coordinate plane over a time step Δt. Using these definitions, equation (6.12) suggests the time-marching algorithm

$$\begin{aligned}\boldsymbol{Q}^{n+1}_{\mathcal{C}} &= \boldsymbol{Q}^n_{\mathcal{C}} - \frac{\Delta t}{V_{\mathcal{C}}} \sum_{i=1}^{n_d} \left(A^i_{\mathcal{C}+}\, \hat{\boldsymbol{F}}^{(i)}_{\mathcal{C}+} - A^i_{\mathcal{C}-}\, \hat{\boldsymbol{F}}^{(i)}_{\mathcal{C}-} \right) \\ &= \boldsymbol{Q}^n_{\mathcal{C}} - \frac{\Delta t\, \widehat{A}^i_{\mathcal{C}}}{\mathcal{V}_{\mathcal{C}}\, \widehat{V}_{\mathcal{C}}} \sum_{i=1}^{n_d} \left(\mathcal{A}^i_{\mathcal{C}+}\, \hat{\boldsymbol{F}}^{(i)}_{\mathcal{C}+} - \mathcal{A}^i_{\mathcal{C}-}\, \hat{\boldsymbol{F}}^{(i)}_{\mathcal{C}-} \right),\end{aligned} \tag{6.15}$$

where the definitions (6.9) have been used in the second equality. Using (6.3) we can write the numerical method as

$$\boldsymbol{Q}^{n+1}_{\mathcal{C}} = \boldsymbol{Q}^n_{\mathcal{C}} - \frac{\Delta t}{\mathcal{V}_{\mathcal{C}}\, \Delta x^i} \sum_{i=1}^{n_d} \left(\mathcal{A}^i_{\mathcal{C}+}\, \hat{\boldsymbol{F}}^{(i)}_{\mathcal{C}+} - \mathcal{A}^i_{\mathcal{C}-}\, \hat{\boldsymbol{F}}^{(i)}_{\mathcal{C}-} \right). \tag{6.16}$$

Notice that the previous numerical method is multidimensional since i ranges from 1 to n_d with $\mathcal{C}^-$ and $\mathcal{C}^-$ representing the "left" and "right" cell edges along x^i, respectively. This numerical method based on flux differences is the starting point for the derivation of a wave propagation algorithm.

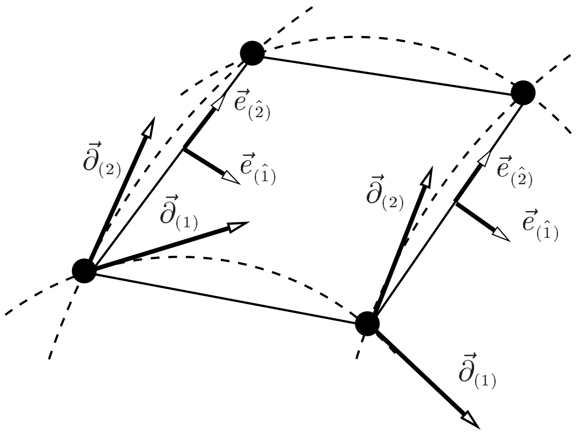

Figure 6.2: The orthonormal frames at each cell edge along x^1. Riemann problems are solved in these orthonormal frames to compute the flux per unit area at each cell interface.

6.3 Orthonormal frames

The numerical method (6.16) updates the solution in the coordinate grid. Therefore, the product $\mathcal{A}^i\,\hat{\boldsymbol{F}}^{(i)}$ should represent flux per coordinate area. Since $\mathcal{A}^i_{\mathcal{C}}$ represents the ratio of physical to coordinate area, $\hat{\boldsymbol{F}}^{(i)}$ represents the flux per unit of physical area through an interface along x^i. One way to be sure that flux per unit physical area is being computed in Riemann problems for a general metric is to locally remove the geometry of $\mathscr{M}$. This is always possible near a point on a manifold at which the metric is not singular.

Recall that in Figure 5.1 a local region of a point in $\mathcal{S}^2$ is represented by a tangent plane on which one can introduce Cartesian coordinates. Though this tangent plane does not represent the global geometry of the sphere, a small region surrounding the tangent point can be described by the Cartesian coordinates on the plane. In these coordinates the metric is the diagonal unit matrix with no spatial dependence. Therefore, the geometry has been locally removed. By solving Riemann problems in such locally Cartesian coordinates, we automatically compute the flux per unit physical area $\hat{\boldsymbol{F}}^{(i)}_{\mathcal{C}}$ needed for the numerical method (6.16). Another benefit to solving Riemann problems in locally Cartesian coordinates is that existing Cartesian solvers can be used. The implementation of such Cartesian solvers in the software package CLAWMAN is discussed in Chapter 7. For the first application of orthonormal coordinates in a general relativistic application see [67].

More will be said about this in Chapter 7.

Figure 6.2 shows a typical finite volume cell for $n_d = 2$. The edges of this cell are straight lines connecting the corner points, and the grid basis is tangent to the coordinate curves as shown in the figure. Flux per unit area, independent of the geometry in $\mathscr{M}$, can be computed in the orthonormal basis vectors $\{\vec{e}_{(\hat{k})}\}$ also depicted in Figure 6.2.

To compute the new basis, we use duality of the coordinate basis and co-basis that was discussed in Section 5.3.1. Figure 5.6 shows the orientation of the co-basis vectors relative to the tangent basis vectors. As the grid shown in Figure 6.2 is refined, the cell edges align with the coordinate curves shown as dashed lines in that figure. In the x^I direction, we would like to have $\vec{e}_{(\hat{I})}$ point in a direction orthogonal to the cell edge, and therefore to the I^{th} coordinate curve C_I. This is exactly the direction that the I^{th} co-basis vector $\tilde{dx}^{(I)}$ points. Recall from equation (5.57) that $|\tilde{dx}^{(I)}| = \sqrt{\tilde{dx}^{(I)} \cdot \tilde{dx}^{(I)}} = \sqrt{h^{II}}$. Using this together with the the fact that the metric provides an isomorphism between the basis and the co-basis (i.e., see Section 5.5), the first orthonormal basis vector can be written

$$\begin{aligned} \vec{e}_{(\hat{I})} &= \frac{\tilde{dx}^{(I)}}{|\tilde{dx}^{(I)}|} = \frac{\tilde{dx}^{(I)}}{\sqrt{h^{II}}} \\ &= \frac{h^{Ij}}{\sqrt{h^{II}}} \vec{\partial}_{(j)}, \end{aligned} \tag{6.17}$$

where x^I is to denote any of the n_d coordinate directions. A capital Latin index is used to signify a fixed index that is not to be summed on. We now have a single unit vector that is orthogonal to the cell interface along the direction x^I. The rest of the orthonormal basis vectors must now be computed.

The second vector in the basis can be chosen to be along $\vec{\partial}_{(J)}$, which is perpendicular to $\vec{e}_{(\hat{I})}$ by duality. This vector can be computed by normalizing $\vec{\partial}_{(J)}$ so that

$$\begin{aligned} \vec{e}_{(\hat{J})} &= \frac{\vec{\partial}_{(J)}}{\sqrt{\vec{\partial}_{(J)} \cdot \vec{\partial}_{(J)}}} \\ &= \frac{\vec{\partial}_{(J)}}{\sqrt{h_{JJ}}}, \end{aligned} \tag{6.18}$$

where the index J is fixed with $J \neq I$. If $n_d = 2$ that is the entire orthonormal set, but for $n_d = 3$ we need another basis vector $\vec{e}_{(\hat{K})}$. This vector must satisfy each of the following criteria:

1. $\vec{e}_{(\hat{K})} \cdot \vec{e}_{(\hat{I})} = 0$; the vector must be orthogonal to the first basis vector.

2. $\vec{e}_{(\hat{K})} \cdot \vec{e}_{(\hat{J})} = 0$; the vector must also be orthogonal to the second basis vector.

3. $\vec{e}_{(\hat{K})} \cdot \vec{e}_{(\hat{K})} = 1$; the vector must have unit length.

One choice that immediately guarantees that (1) is satisfied is

$$\vec{e}_{(\hat{K})} = \alpha\, \vec{\partial}_{(J)} + \beta\, \vec{\partial}_{(K)}. \tag{6.19}$$

The second two criteria are satisfied if α and β represent solutions to the following algebraic system

$$\alpha \sqrt{h_{JJ}} + \frac{\beta\, h_{JK}}{\sqrt{h_J J}} = 0 \tag{6.20}$$

$$\alpha^2\, h_{JJ} + \beta^2\, h_{KK} + 2\, \alpha\, \beta\, h_{JK} = 1. \tag{6.21}$$

Table 6.1: The role of the indices I, J, and K for each direction in which Riemann problems are solved.

directions	values I	J	K
x^1	1	2	3
x^2	2	1	3
x^3	3	1	2

The first equation has solution

$$\alpha = -\frac{h_{JK}}{h_{JJ}}\beta, \tag{6.22}$$

and will be finite for a well behaved metric tensor since $h_{JJ} \neq 0$. This can be used in equation (6.21) to give

$$\beta^2 \left(h_{JJ}\, h_{KK} - (h_{JK})^2 \right) = h_{JJ}, \tag{6.23}$$

which can immediately be solved for β. Notice, however, that the quantity inside the braces in the previous equation is just the determinant of the restricted metric tensor, $\overset{\leftrightarrow}{h}{}^{\perp^I}_{ij}$, that was discussed in the previous section. Using this we can write the solution for β as

$$\beta = \frac{\sqrt{h_{JJ}}}{\sqrt{h^{\perp^I}}}. \tag{6.24}$$

Therefore, the set of orthonormal basis vectors along the x^I direction can be written

$$\left\{ \vec{e}_{(\hat{I})}, \vec{e}_{(\hat{J})}, \vec{e}_{(\hat{K})} \right\} = \left\{ \frac{h^{Ij}}{\sqrt{h^{II}}}\vec{\partial}_{(j)}\,,\ \frac{1}{\sqrt{h_{JJ}}}\vec{\partial}_{(J)}\,,\ -\frac{h_{JK}}{\sqrt{h_{JJ}}\,\sqrt{h^{\perp^I}}}\vec{\partial}_{(J)} + \frac{\sqrt{h_{JJ}}}{\sqrt{h^{\perp^I}}}\vec{\partial}_{(K)} \right\}, \tag{6.25}$$

where $I \neq J \neq K$.

The set of vectors (6.25) derived above represents an orthonormal basis for any choice of I, J, and K as long as they are different. Once I is set by the direction in which Riemann problems are being solved, however, the construction of $\vec{e}_{(\hat{J})}$ and $\vec{e}_{(\hat{K})}$ depends on the particular choice of J and K. In two space dimensions there is, of course, only one choice for J once I is set. In this case the basis defined in (6.25) is unique. In three dimensions, however, one must make a choice for J. For example, if $I = 1$, then J can be 2 or 3 with either choice resulting in a perfectly valid orthonormal basis. Table 6.1 shows the particular choice for the indices I, J, and K in the algorithm used here. This particular choice is made so that the transformation matrices in two dimensions look identical to the three dimensional transformations with one less row and column. Notice that in Table 6.1 I is always chosen to be the index of the direction in which Riemann problems are being solved.

In order to solve Riemann problems in the orthonormal basis in (6.25), it is necessary to transform both tangent and cotangent vector components into that frame. The matrix O^I is defined as the transformation matrix satisfying

$$\left[v^{\hat{k}}\right] = \left[O^{\hat{k}}_j\right]\left[v^j\right], \tag{6.26}$$

where $v^{\hat{k}}$ represents the components of $\vec{v}$ in the orthonormal frame. Since the basis (6.25) represents $\vec{e}_{(\hat{k})}$ as a linear combination of the canonical basis vectors, equation (5.14) can be used to write down the elements of the transformation matrix. Along the $\vec{\partial}_{(1)}$ direction we take $I = 1$, $J = 2$, and $K = 3$ so that equation (5.25) gives

$$\left[\Pi^{\hat{k}}_j\right] = \begin{pmatrix} \sqrt{h^{11}} & 0 & 0 \\ \frac{h^{12}}{\sqrt{h^{11}}} & \frac{1}{\sqrt{h_{22}}} & -\frac{h_{23}}{\sqrt{h_{22}}\sqrt{h^{\perp 1}}} \\ \frac{h^{13}}{\sqrt{h^{11}}} & 0 & \frac{h_{22}}{\sqrt{h^{\perp 1}}} \end{pmatrix}. \tag{6.27}$$

Using equation (5.17) together with the previous matrix, the transformation matrix that takes tangent vector components from the grid basis to the orthonormal basis along the x^1 direction can be written

$$\left[O^{\hat{k}}_j\right]^1 = \left[\Pi^{\hat{k}}_j\right]^{-1} = \begin{pmatrix} \frac{1}{\sqrt{h^{11}}} & 0 & 0 \\ \frac{h_{12}}{\sqrt{h_{22}}} & \sqrt{h_{22}} & \frac{h_{23}}{\sqrt{h_{22}}} \\ -\frac{h^{13}\sqrt{h^{\perp 1}}}{\sqrt{h^{11}}\sqrt{h_{22}}} & \frac{h_{23}}{\sqrt{h_2 2}} & \frac{\sqrt{h^{\perp 1}}}{\sqrt{h_{22}}} \end{pmatrix}. \tag{6.28}$$

The transformation matrices in the other directions can be computed in a similar way using Table 6.1 together with equation (6.25). The transformation matrix in the x^2 direction is

$$\left[O^{\hat{k}}_j\right]^2 = \begin{pmatrix} \sqrt{h_{11}} & \frac{h_{12}}{\sqrt{h_{11}}} & \frac{h_{13}}{\sqrt{h_{11}}} \\ 0 & \frac{1}{\sqrt{h^{22}}} & 0 \\ 0 & -\frac{h^{23}\sqrt{h^{\perp 2}}}{\sqrt{h^{22}}\sqrt{h_{11}}} & \frac{h^{\perp 2}}{\sqrt{h_1 1}} \end{pmatrix}, \tag{6.29}$$

and in the x^3 direction it has the form

$$\left[O^{\hat{k}}_j\right]^3 = \begin{pmatrix} \sqrt{h_{11}} & \frac{h_{12}}{\sqrt{h_{11}}} & \frac{h_{13}}{\sqrt{h_{11}}} \\ 0 & \frac{h^{\perp 3}}{\sqrt{h^{11}}} & -\frac{h^{32}\sqrt{h^{\perp 3}}}{\sqrt{h^{33}}\sqrt{h_{11}}} \\ 0 & 0 & \frac{1}{\sqrt{h^{33}}} \end{pmatrix}. \tag{6.30}$$

It was previously mentioned that all the examples in this thesis are done in manifolds with $n_d = 2$. The transformation matrices in that case are simply the first two rows and columns of the matrices above.

6.4 Scalar conservation laws

Let us first develop the algorithm for a scalar conservation law of the form (5.83). Consider the scalar advection equation

$$q(t,\vec{x})_{,t} + \vec{\nabla}\cdot q\,\vec{u} = 0, \tag{6.31}$$

in which the concentration q is advected with velocity $\vec{v}$. Using equation (5.83), this equation can be written on the coordinate basis of the finite volume grid as

$$q(t,x^k)_{,t} + \frac{1}{\sqrt{h}}\left(\sqrt{h}\,q\,u^i\right)_{,i} = 0, \tag{6.32}$$

where, once again, a subscript following a comma denotes a partial derivative and a sum is implied on repeated indices if one is up and the other down. Since this equation is scalar, there is no source term generated by the geometry. In this case, the algorithm only needs to handle the spatially-varying flux in equation (6.32). We have already discussed the details of a wave propagation algorithm based on f-waves in Chapter 3 and in the recent paper [4]. The f-waves were shown to handle spatially-varying flux functions both efficiently and accurately. The application of f-waves on manifolds is now developed.

The finite volume approximation, $\boldsymbol{Q}^n_{|ij}$, will be defined by the cell average (6.13) with $n_d = 2$. The discretized spatially-varying flux has the form

$$\boldsymbol{f}^{(k)}_{|ij}(\boldsymbol{Q}_{|ij}) = \mathcal{V}_{|ij}\,\boldsymbol{Q}_{|ij}\,u^k_{|ij}, \tag{6.33}$$

where the velocity components $u^k_{|ij}$ are discretized at cell centers so that

$$u^k_{|ij} = u^k(x^1_i, x^2_j), \tag{6.34}$$

and the point (x^1_i, x^2_j) is at the center of $\mathcal{C}_{ij}$. For the discussion here, we consider a velocity such that $u^k_{|ij} > 0$ throughout the grid.

The method developed here is based on solving one-dimensional Riemann problems along each coordinate direction in the orthonormal frames discussed in the previous section. Since equation (6.32) is scalar, the eigenvectors in each direction needed for a decomposition in the Riemann solution are simply $r^p = 1$ and have no geometric information associated with them. The eigenvalues suggested by (6.33), however, have the form

$$\lambda^k = \sqrt{h}\,u^k, \tag{6.35}$$

which contains information about the geometry through the determinant of the metric. Therefore, in order to compute $\hat{\boldsymbol{F}}^{(k)}$, we transform to an orthonormal frame.

Consider the Godunov numerical fluxes $\hat{\boldsymbol{F}}^{(1)}_{|i-1/2,j}$, and $\hat{\boldsymbol{F}}^{(1)}_{|i+1/2,j}$ that result from solving Riemann problems along x^1 in the orthonormal frames at the left and right edges of $\mathcal{C}_{ij}$, respectively. Since the velocity is everywhere positive, they have the form

$$\begin{aligned}\hat{\boldsymbol{F}}^{(\hat{1})}_{|i-1/2,j} &= \boldsymbol{Q}_{|i-1,j}\,u^{\hat{1}}_{|i-1,j},\\ \hat{\boldsymbol{F}}^{(\hat{1})}_{|i+1/2,j} &= \boldsymbol{Q}_{|ij}\,u^{\hat{1}}_{|ij}.\end{aligned} \tag{6.36}$$

These fluxes represent the flux per unit area, but the are written in terms of the orthonormal tangent components. At the left edge of the cell, these components can be written in terms of the canonical components using the fact that

$$\begin{aligned} u^{\hat{1}}_{|i-1/2,j} = \vec{e}_{(\hat{1})} \cdot \vec{v}_{|i-1,j} &= \frac{\tilde{dx}^{(1)}}{\sqrt{h^{11}}_{|i-1,j}} \cdot \vec{v}_{|i-1,j} \\ &= \frac{v^1_{|i-1,j}}{\sqrt{h^{11}}_{|i-1,j}}. \end{aligned} \tag{6.37}$$

Similarly, $u^{\hat{1}}_{|i+1/2,j}$ at the right edge is defined so that

$$u^{\hat{1}}_{|i+1/2,j} = \frac{v^1_{ij}}{\sqrt{h^{11}}_{|ij}}. \tag{6.38}$$

The flux per unit area along the left and right edges of the cell can now be rewritten in terms of the coordinate velocity components as

$$\begin{aligned} \hat{\boldsymbol{F}}^{(1)}_{|i-1/2,j} &= \frac{\boldsymbol{Q}_{|i-1,j}\, u^1_{|i-1,j}}{\sqrt{h^{11}}_{|i-1,j}}, \\ \hat{\boldsymbol{F}}^{(1)}_{|i+1/2,j} &= \frac{\boldsymbol{Q}_{|ij}\, u^1_{|ij}}{\sqrt{h^{11}}_{|ij}}. \end{aligned} \tag{6.39}$$

Using these numerical fluxes together with the fluxes in the x^2 direction denoted by $\hat{\boldsymbol{F}}^{(2)}_{|i,j-1/2}$ and $\hat{\boldsymbol{F}}^{(2)}_{|i,j+1/2}$, the numerical method (6.16) can be written

$$\begin{aligned} \boldsymbol{Q}^{n+1}_{|ij} = \boldsymbol{Q}^n_{|ij} &- \frac{\Delta t}{\mathcal{V}_{|ij}\,\Delta x^1}\left(\frac{\mathcal{A}^1_{|ij}}{\sqrt{h^{11}}_{|ij}}\boldsymbol{Q}_{|ij}\, u^1_{|ij} - \frac{\mathcal{A}^1_{|i-1,j}}{\sqrt{h^{11}}_{|i-1,j}}\boldsymbol{Q}_{|i-1,j}\, u^1_{|i-1,j}\right) \\ &- \frac{\Delta t}{\mathcal{V}_{|ij}\,\Delta x^2}\left(\frac{\mathcal{A}^2_{|ij}}{\sqrt{h^{22}}_{|ij}}\boldsymbol{Q}_{|ij}\, u^2_{|ij} - \frac{\mathcal{A}^2_{|i,j-1}}{\sqrt{h^{22}}_{|i,j-1}}\boldsymbol{Q}_{|i,j-1}\, u^2_{|i,j-1}\right). \end{aligned} \tag{6.40}$$

Using equation (6.10) that relates the components of the inverse metric tensor to the ratios defined in equation (6.9), we can write the previous numerical update as

$$\begin{aligned} \boldsymbol{Q}^{n+1}_{|ij} &= \boldsymbol{Q}^n_{|ij} - \frac{\Delta t}{\mathcal{V}_{|ij}\,\Delta x^1}\left(\mathcal{V}_{|ij}\,\boldsymbol{Q}_{|ij}\, u^1_{|ij} - \mathcal{V}_{|i-1,j}\,\boldsymbol{Q}_{|i-1,j}\, u^1_{|i-1,j}\right) \\ &\quad - \frac{\Delta t}{\mathcal{V}_{|ij}\,\Delta x^2}\left(\mathcal{V}_{|ij}\,\boldsymbol{Q}_{|ij}\, u^2_{|ij} - \mathcal{V}_{|i,j-1}\,\boldsymbol{Q}_{|i,j-1}\, u^2_{|i,j-1}\right) \end{aligned} \tag{6.41}$$

$$\begin{aligned} &= \boldsymbol{Q}^n_{|ij} - \frac{\Delta t}{\mathcal{V}_{|ij}\,\Delta x^1}\left(\boldsymbol{f}^{(1)}_{|ij}(\boldsymbol{Q}_{|ij}) - \boldsymbol{f}^{(1)}_{|i-1,j}(\boldsymbol{Q}_{|i-1,j})\right) \\ &\quad - \frac{\Delta t}{\mathcal{V}_{|ij}\,\Delta x^2}\left(\boldsymbol{f}^{(2)}_{|ij}(\boldsymbol{Q}_{|ij}) - \boldsymbol{f}^{(2)}_{|i,j-1}(\boldsymbol{Q}_{|i,j-1})\right), \end{aligned} \tag{6.42}$$

where we have used the definition of the cell-centered flux (6.33) in the last equality. Recall that in equation (3.12) it was precisely those flux differences found in the previous update (6.42) that are decomposed into f-waves, $\{\boldsymbol{\mathcal{Z}}^p\}$. In the example used here, a single f-wave propagates in each direction, one from the left edge of the cell $\boldsymbol{\mathcal{Z}}^1_{|i-1/2,j}$, and the other from the lower edge of the cell $\boldsymbol{\mathcal{Z}}^1_{|i,j-1/2}$.

For a system of n_{eq} scalar equations, the flux difference is decomposed into a set of n_{eq} f-waves. In the x^1 direction, for example, this decomposition takes the form

$$\boldsymbol{f}^{(k)}_{|ij}(\boldsymbol{Q}_{|ij}) - \boldsymbol{f}^{(k)}_{|i-1,j}(\boldsymbol{Q}_{|i-1,j}) = \sum_{p=1}^{n_{eq}} \boldsymbol{\mathcal{Z}}^p_{|i-1/2,j}, \tag{6.43}$$

and a similar decomposition exists in the x^2 direction. These decompositions allow us to replace the right hand side of the update (6.42) by fluctuations that are based on these f-waves. In this way, the numerical method (6.16) that is based on flux differences can be written as the wave propagation algorithm

$$\boldsymbol{Q}^{n+1}_{\mathcal{C}} = \boldsymbol{Q}^n_{\mathcal{C}} - \frac{\Delta t}{\mathcal{V}_{\mathcal{C}}\,\Delta x^i} \sum_{i=1}^{n_d} \left(\boldsymbol{\mathcal{A}}^+_i \boldsymbol{\Delta Q}_{\mathcal{C}^-} + \boldsymbol{\mathcal{A}}^-_i \boldsymbol{\Delta Q}_{\mathcal{C}^+} \right), \tag{6.44}$$

based on f-waves. In the last equation, as previously explained, the notation $\mathcal{C}^{\pm}$ refers to the left or right edge of the cell along the direction x^i. The fluctuations are defined in terms of f-waves as

$$\begin{aligned} \boldsymbol{\mathcal{A}}^- \boldsymbol{\Delta Q}_{\mathcal{C}^-} &= \sum_{p \in \mathscr{P}^-} \boldsymbol{\mathcal{Z}}^p_{\mathcal{C}^-} \\ \boldsymbol{\mathcal{A}}^+ \boldsymbol{\Delta Q}_{\mathcal{C}^-} &= \sum_{p \in \mathscr{P}^+} \boldsymbol{\mathcal{Z}}^p_{\mathcal{C}^-}, \end{aligned} \tag{6.45}$$

as they were in Chapter 3. High-resolution corrections and transverse propagation is handled in the same manner that it was in Chapter 3.

6.4.1 Wave speeds

The speed at which the wave travels in the x^k direction should approximate the eigenvalue $s^1 \approx \sqrt{h}\, u^k$. For the advection example that we are considering here, the speed is set based on the eigenvalue in the cell that the wave will propagate into so that

$$s^1_{|i-1/2,j} = \mathcal{V}_{|ij}\, u^1_{|ij}. \tag{6.46}$$

Recall from equation (3.20) that the original waves that carry jumps in q can be computed from the f-waves and speeds (as long as $s \neq 0$) using the fact that $\boldsymbol{\mathcal{W}}^1_{|i-1/2,j} = \boldsymbol{\mathcal{Z}}^1_{|i-1/2,j} / s^1_{|i-1/2,j}$. In this case $\boldsymbol{\mathcal{W}}^1_{|i-1/2,j}$ has a wave strength

$$\begin{aligned} \boldsymbol{\mathcal{W}}^1_{|i-1/2,j} = \frac{\boldsymbol{\mathcal{Z}}^1_{|i-1/2,j}}{s^1_{|i-1/2,j}} &= \frac{\mathcal{V}_{|ij}\, u^1_{|ij}\, \boldsymbol{Q}_{|ij} - \mathcal{V}_{|i-1,j}\, u^1_{|i-1,j}\, \boldsymbol{Q}_{|i-1,j}}{\mathcal{V}_{|ij}\, u^1_{|ij}} \\ &= \boldsymbol{Q}_{|ij} - \frac{\mathcal{V}_{|i-1,j}\, u^1_{|i-1,j}}{\mathcal{V}_{|ij}\, u^1_{|ij}} \boldsymbol{Q}_{|i-1,j}. \end{aligned} \tag{6.47}$$

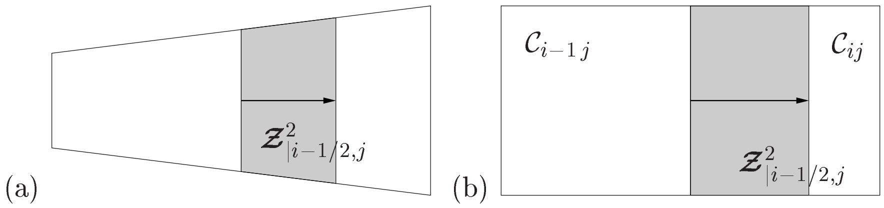

Figure 6.3: (a) Two f-waves traveling into cells $\mathcal{C}_{i-1\,j}$ and $\mathcal{C}_{ij}$ in the coordinate grid. (b) The same two f-waves traveling on the physical grid where it is clear the right-traveling wave is entering a cell with larger *volume*.

Let us suppose for a moment that the velocity is constant so that $u^1_{|i-1,j} = u^1_{|ij} > 0$, and material is flowing into the right cell so that $Q_{|i-1,j} > Q_{|ij}$. The wave propagates through the coordinate grid as depicted in Figure 6.3(b), and maps to the physical wave shown in Figure 6.3(a). A method that simply propagates a concentration wave with strength $Q_{|ij} - Q_{|i-1,j}$ into the right cell that has larger volume will update that cell with too much material. In reality, as the wave propagates into the right cell it has to fill more volume, hence the concentration decreases.

Equation (6.47) shows that for the method presented here based on f-waves, the wave propagating into the right cell will have strength

$$\mathcal{W}^1_{|i-1/2,j} = Q_{|ij} - \frac{\mathcal{V}_{|i-1,j}}{\mathcal{V}_{|ij}} Q_{|i-1,j}, \tag{6.48}$$

which is smaller than the full jump since $\mathcal{V}_{|i-1,j}/\mathcal{V}_{|ij} < 1$. Solving Riemann problems using f-waves, therefore, produces waves with geometry encoded into them and the geometry determines the strength of the waves that propagate.

6.4.2 Advection in a polar basis

In this section, we apply the numerical method (6.44) to the advection of a concentration subject to a radially symmetric velocity field. The manifold is taken to be a flat two dimensional plane, $\mathscr{M} = \mathbb{R}^2$, covered by polar coordinates $\{r, \theta\}$. These coordinates are related to the Cartesian coordinates using

$$\begin{aligned} x(r,\theta) &= r\,\cos\theta \\ y(r,\theta) &= r\,\sin\theta, \end{aligned} \tag{6.49}$$

in the usual way. The covariant components of the metric tensor in polar coordinates can be calculated using the transformation rule (5.50) with $x^i = \{x, y\}$ and $x^{\bar{k}} = \{r, \theta\}$. The elements (5.25) of the transformation form the matrix

$$\left[\Pi^j_{\bar{k}}\right] = \begin{pmatrix} \cos\theta & -r\,\sin\theta \\ \sin\theta & r\,\cos\theta \end{pmatrix}. \tag{6.50}$$

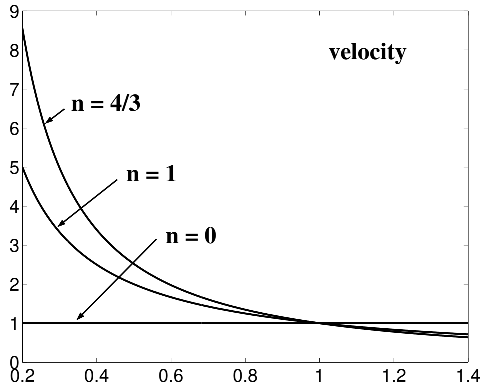

Figure 6.4: Radially symmetric velocity field used in advection example. The velocity becomes large and positive for small values of r with increasing n.

Using this matrix in the transformation defined by (5.50) together with the fact that the metric in Cartesian coordinates is $h_{ij} = \mathrm{diag}(1,1)$, the metric in polar coordinates can be written

$$[h_{ij}] = \mathrm{diag}(1, r^2). \tag{6.51}$$

In the previous equation, the over-bar notation has been dropped and it is assumed that $x^i = \{r, \theta\}$. The determinant of the polar metric is $h = r^2$, so the volume element on the polar grid is given by

$$V_{|ij} = r_{|ij}\, \Delta r\, \Delta\theta, \tag{6.52}$$

which is independent of θ.

In this example an initial condition that is independent of θ is used together with a radially symmetric velocity field. Therefore, the solution should remain independent of θ. The radially symmetric velocity field has the form

$$\vec{v} = \alpha\, r^{-n}\, \vec{\partial}_{(r)}, \tag{6.53}$$

where both α and n are constants. If $n = 0$ then α is the amplitude of a constant outflow. As n increases, the outflow becomes stronger for smaller r as shown in Figure 6.4. The particular values of n in the figure, $\{0, 1, 4/3\}$, are the values for which we compute solutions using this velocity field.

The initial condition used for $q(t, r, \theta)$ is independent of θ and has the form

$$q(t=0, r) \equiv f(r) = \begin{cases} \frac{1}{2}\, a \left(\cos \frac{\pi(r - r_0)}{\omega} + 1\right) & \text{if } |r - r_0| < \omega \\ 0 & \text{if } |r - r_0| > \omega, \end{cases} \tag{6.54}$$

where a is the peak concentration, r_0 is the radius at which this peak occurs, and ω is a measure of the width of the concentration. Equation (6.31), together with this initial

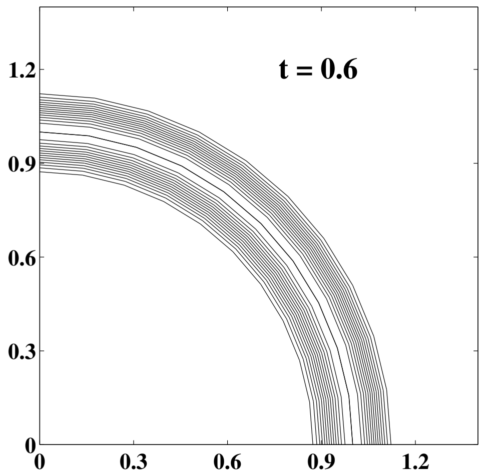

(a) n=0

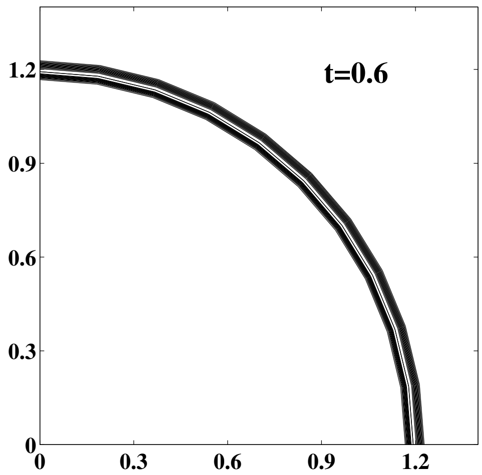

(b) n=4/3

Figure 6.5: (a) Contours of the concentration at $t = 0.6$ for $n = 0$. (b) Contours of the concentration at $t = 0.6$ for $n = 4/3$.

condition, can be exactly solved for a general n using the method of characteristics. The solution can be written in the explicit form

$$q(t,r,\theta) = \begin{cases} f\left(\left[r^2 - 2\,\alpha\,t\right]^{1/2}\right) & \text{if } n = 1 \\ r^{n-1}\,\left[r^{n+1} - \alpha\,(n+1)\,t\right]^{\frac{1-n}{1+n}}\, f\left(\left[r^{n+1} - \alpha\,(n+1)\,t\right]^{\frac{1}{1+n}}\right) & \text{if } n \neq 1 \end{cases}. \tag{6.55}$$

The reason this velocity field was chosen is that the geometric spreading of concentration can be eliminated, and in fact, overtaken by the fact that the velocity changes with r. For example, let $n = 0$ in the solution (6.55) to find $q = (1 - \alpha\,t/r) f(r - \alpha\,t)$. As time progresses, the wave propagates to larger values of r and the solution decays. This is exactly what we should expect since $n = 0$ corresponds to a constant outflow. The same amount of material at larger r is filling more space in $\mathscr{M}$, hence the concentration decreases. However, if $n = 1$, then the amount by which the concentration is geometrically decreased is exactly balanced by the fact that the flow slows down as r increases. The fact that the flow slows means that material will pile up. For $n = 1$ these two effects exactly balance each other so that the amplitude remains constant. Finally, when $n > 1$ the rate at which material piles up as the wave travels to larger r is of greater influence than the geometric spreading of the wave. In this case, the concentration increases as the wave propagates outward.

Though the solutions for each n are functions only of r, the calculations have been done in two space dimensions so that we can test the radial symmetry of the method. Figures 6.16(a) and 6.16(b) show the two-dimensional contours of the concentration at $t = 0.6$ for $n = 0$ and $n = 4/3$. The squeezing of the material can be seen by the width of the contours

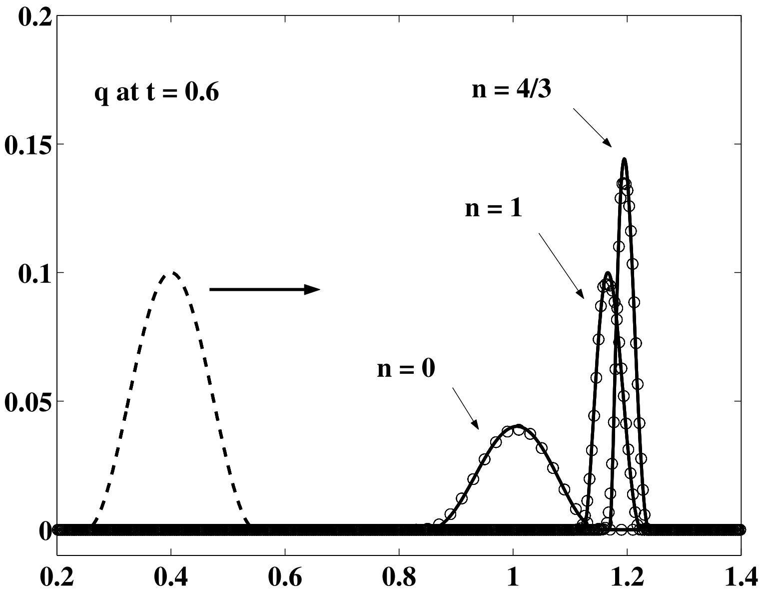

Figure 6.6: The exact solution at $t = 0.6$ for each $n \in \{0, 1, 4/3\}$ is represented by the solid lines. The initial condition is shown as a dashed line. A scatter plot of the computed solution is also shown for each n as circles.

in Figure 6.16(b). The radial profile of the initial condition (6.77) that has been used can be seen as the dashed line in Figure 6.6. The exact solutions for each $n \in \{0, 1, 4/3\}$ are represented by solid lines in this same figure. The circles represent a scatter plot of each data point in the two-dimensional calculations shown in Figures 6.16(a) and 6.16(b). The fact that there is no scatter in those points confirms that the data is radially symmetric. The computed values agree with the exact solution. Figure 6.7 is a plot of the one norm of the error for the solution with $n = 0$. It is clear that the method is second order on this problem.

6.5 Vector conservation laws

So far, we have discussed the use of f-waves that handle the spatially-varying flux that appears for conservation laws on manifolds. These f-waves induce fluctuations that are used in the update (6.44). In this section, the algorithm is generalized to handle vector conservation laws. In the next section, the systems consisting of both scalar and vector laws are discussed.

In Section 5.8.2 we saw that a vector conservation law on a manifold can be written in the form

$$v^j_{,t} + \frac{1}{\sqrt{h}} \left(\sqrt{h}\, T^{kj} \right)_{,k} = -\Gamma^j_{mk} T^{mk}, \tag{6.56}$$

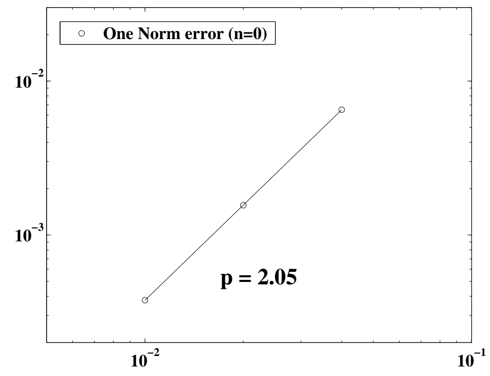

Figure 6.7: A plot of the one norm for the error in the computed solution with $n = 0$. The order has been computed to be 2.05.

where v^j are the tangent components of the conserved vector $\vec{v}$, and T^{ij} are the tangent components of $\overset{\leftrightarrow}{T}$, a second rank symmetric (i.e. $\overset{\leftrightarrow}{T}(\tilde{e}^{(i)}, \tilde{e}^{(j)}) = \overset{\leftrightarrow}{T}(\tilde{e}^{(j)}, \tilde{e}^{(i)})$) flux tensor. Recall that the Christoffel symbols in equation (6.56), denoted by Γ^i_{jk}, represent components of the derivatives of the canonical basis $\{\vec{\partial}_{(k)}\}$.

The new feature of a vector conservation law is that the quantity being conserved depends on the basis. This fact is not a problem when the basis vectors are independent of the coordinates as they are in a Cartesian basis. However, when the basis is spatially varying as it is in a general manifold, a meaningful comparison of the same component v^j at two distinct locations in $\mathscr{M}$ must be made with reference to only a single basis. This was not true for scalar equations because a scalar does not need to be measured against any basis vector. The fact that there is a different set of basis vectors at each point of $\mathscr{M}$ did not affect the scalar fields.

In Section 5.7, the parallel transport of vector components along a general curve was introduced. If the curve along which we parallel transport the components of a vector $\vec{v}$ is a coordinate curve C_k, then the fact that $\dot{x}^i = \delta^i_k$ along this curve allows us to write equation (5.73) as

$$\begin{aligned} v^j_{;k} &= v^j_{,k} + v^m\,\Gamma^j_{mk} \\ &= 0. \end{aligned} \tag{6.57}$$

If we start with a vector component, v^j, at some point $\mathcal{P} \in \mathscr{M}$ with components $(x^1_0, \cdots, x^{n_d}_0)$, and parallel transport that component to a nearby point separated from $\mathcal{P}$ by Δx^k along C_k, then the new components according to the ODE (6.57) will be

$$v^j = v^j(\mathcal{P}) - \int_{x^k_0}^{x^k_0 + \Delta x^k} v^m\,\Gamma^j_{mk}\,dx^k. \tag{6.58}$$

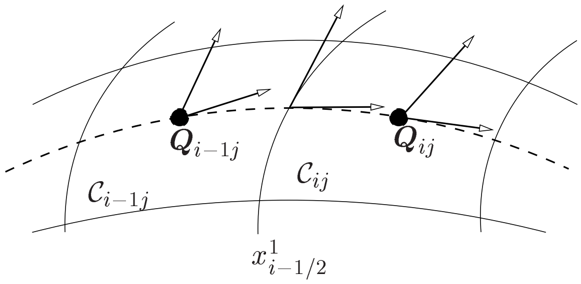

Figure 6.8: The basis vectors at the centers of cells $\mathcal{C}_{i-1j}$ and $\mathcal{C}_{ij}$ are different than the basis at the cell edge. Vector and tensor components must be parallel propagated to the basis at the cell edge.

The components of $\vec{v}$ are only changing to compensate for the fact that the basis has changed at the new point. In effect, the component is simply being projected into the basis at the new point without changing itself.

The tangent components of a tensor suffer the same problem as those discussed for vector components. The source term, $-T^{mn}\,\Gamma^j_{mn}$, that appears in equation (6.56) is due to the fact that the spatially separated components of the flux tensor that are needed for the derivatives in the divergence must be projected into the same coordinate basis before a meaningful difference can be taken. One of the main novel features of the algorithm presented here is that the source term in equation (6.56) is handled using parallel transport of vector components.

6.5.1 Discrete parallel transport

Figure 6.8 shows a typical coordinate grid for $n_d = 2$ with different bases at each of the cell centers and the cell interface. Suppose that we are solving the momentum equation for a fluid (see Appendix B for the equations) so that components of the state vector $\boldsymbol{Q}$ and flux $\boldsymbol{f}^{(k)}$ involve the momentum components $\rho\, v^k$. Typically, Riemann problems at each cell interface are based on decomposing the difference between such components located at the centers of the contiguous cells shown in Figure 6.8. Because this difference involves two different sets of bases, the source term in equation (6.56) must also be incorporated.

Instead, the method proposed here parallel propagates vector components of $\boldsymbol{Q}$ to the cell interface prior to the solution of Riemann problems. In this way, as we will show, the source term is locally incorporated into each Riemann problem. By doing so, we hope to avoid problems discussed in Chapter 4.

In Section 5.7, the discrete parallel transport of vector components along general curves was derived and written in the form

$$\left[s^i\right]_{\mathcal{Q}} = \left[P^i_m\right]\, \left[s^m\right]_{\mathcal{P}}\,, \tag{6.59}$$

where the two points $\mathcal{P}$ and $\mathcal{Q}$ are on the curve. Since only one-dimensional Riemann problems are solved in the algorithm developed here, the curves along which parallel transport must take place are the coordinate curves C_k. This being the case, the elements of the discrete parallel propagation matrix, $\left[P^i_m\right]$ along the K^{th} coordinate curve will have the form

$$P^i_m = \delta^i_m - \Delta x^K\,\Gamma^i_{mK} + \frac{1}{2}\left(\Delta x^K\right)^2\left(\Gamma^i_{nK}\,\Gamma^n_{Km} - \mathcal{G}^i_{mKK}\right) + \mathcal{O}\left((\Delta x^K)^3\right), \tag{6.60}$$

where, once again, the use of a capital Latin index signifies that it is a single number and never to be summed, and $\mathcal{G}^i_{mKK}$ represents the partial derivative of Γ^i_{mK} along C_K. The direction along C_K that the components are propagated depends on the sign of Δx^K. For $\Delta x^K < 0$, components are parallel propagated to the left, but for $\Delta x^K > 0$, they are propagated to the right.

Generalizing the discrete flux defined in (6.33), the cell-centered discretization of the flux is defined to be

$$\boldsymbol{f}^{(k)}_{|ij}(\boldsymbol{Q}_{|ij}) = \mathcal{V}_{|ij}\,\boldsymbol{f}^{(k)}(\boldsymbol{Q}_{|ij}). \tag{6.61}$$

As mentioned above, simply decomposing the difference of this flux at each cell interface into a set of f-waves would yield a difference of vector components at spatially separated points. Doing so would also require that the source on the right side of (6.56) be incorporated in some way. Instead, the source can be absorbed into the Riemann problem by taking a flux difference between the modified fluxes defined by

$$\boldsymbol{f}^{(1)-}_{|ij} = [P]^-_{ij}\,\boldsymbol{f}^{(1)}_{|ij}; \quad \text{modified right flux} \tag{6.62}$$

$$\boldsymbol{f}^{(1)+}_{|i-1,j} = [P]^+_{i-1,j}\,\boldsymbol{f}^{(1)}_{|i-1,j}; \quad \text{modified left flux,} \tag{6.63}$$

where $[P]^-_{ij}$ parallel propagates vector components of $\boldsymbol{f}^{(1)}_{|ij}$ to the left edge of $\mathcal{C}_{ij}$, and $[P]^+_{i-1,j}$ propagates $\boldsymbol{f}^{(1)}_{|i-1,j}$ to the right edge of $\mathcal{C}_{i-1,j}$. Similar modifications take place in the other spatial directions. The result is a flux difference at the cell edge for which both left and right fluxes are expressed in the same basis. The Riemann problem will involve the modified data.

A calculation computing the influence of parallel propagation on the flux difference shows that differencing the modified fluxes incorporates the source term in present equation (6.56). If terms higher than first order are neglected, one finds that

$$\begin{aligned}
\boldsymbol{f}^{(1)-}_{|ij} - \boldsymbol{f}^{(1)+}_{|i-1,j} &= [P]^-_{ij}\,\boldsymbol{f}^{(1)}_{|ij} - [P]^+_{i-1,j}\,\boldsymbol{f}^{(1)}_{|i-1,j} \\
&= \left(\mathcal{I} + \frac{\Delta x^1}{2}\Gamma^i_{m1|ij}\right)\boldsymbol{f}^{(1)m}_{|ij} - \left(\mathcal{I} - \frac{\Delta x^1}{2}\Gamma^i_{m1|i-1,j}\right)\boldsymbol{f}^{(1)m}_{|i-1,j} \\
&= \boldsymbol{f}^{(1)m}_{|ij} - \boldsymbol{f}^{(1)m}_{|i-1,j} - \Delta x^1\,\frac{1}{2}\left(\Gamma^i_{n1|i-1,j}\boldsymbol{f}^{(1)n}_{|i-1,j} + \Gamma^i_{n1|ij}\boldsymbol{f}^{(1)n}_{|ij}\right),
\end{aligned} \tag{6.64}$$

along the x^1 direction, and that

$$\begin{aligned}
\boldsymbol{f}^{(2)-}_{|ij} - \boldsymbol{f}^{(2)+}_{|i,j-1} &= [P]^-_{ij}\,\boldsymbol{f}^{(2)}_{|ij} - [P]^+_{i,j-1}\,\boldsymbol{f}^{(2)}_{|i,j-1} \\
&= \left(\mathcal{I} + \frac{\Delta x^2}{2}\Gamma^i_{m2|ij}\right)\boldsymbol{f}^{(2)m}_{|ij} - \left(\mathcal{I} - \frac{\Delta x^2}{2}\Gamma^i_{m2|i,j-1}\right)\boldsymbol{f}^{(2)m}_{|i,j-1} \\
&= \boldsymbol{f}^{(2)m}_{|ij} - \boldsymbol{f}^{(2)m}_{|i,j-1} - \Delta x^2\,\frac{1}{2}\left(\Gamma^i_{n2|i,j-1}\boldsymbol{f}^{(2)n}_{|i,j-1} + \Gamma^i_{n2|ij}\boldsymbol{f}^{(2)n}_{|ij}\right),
\end{aligned} \tag{6.65}$$

along the x^2 coordinate. The average that appears in both modified flux differences suggests that we define

$$\begin{aligned}\boldsymbol{\psi}^{(1)}_{|i-1/2,j} &\equiv \frac{1}{2}\left(\Gamma^i_{n1|i-1,j}\boldsymbol{f}^{(1)n}_{|i-1,j} + \Gamma^i_{n1|ij}\boldsymbol{f}^{(1)n}_{|ij}\right)\\ \boldsymbol{\psi}^{(2)}_{|i,j-1/2} &\equiv \frac{1}{2}\left(\Gamma^i_{n2|i,j-1}\boldsymbol{f}^{(2)n}_{|i,j-1} + \Gamma^i_{n2|ij}\boldsymbol{f}^{(2)n}_{|ij}\right)\end{aligned} \tag{6.66}$$

at the cell edges. If these definitions are used in the flux differences (6.64) and (6.65), then they look just like the modified flux difference (4.42) for the source term method discussed in Section 4.2.

Notice that through both x^1 and x^2 sweeps through the grid, a source term of the form

$$\boldsymbol{\psi} = \Gamma^i_{11}\boldsymbol{f}^{(1)1} + \Gamma^i_{21}\boldsymbol{f}^{(1)2} + \Gamma^i_{12}\boldsymbol{f}^{(2)1} + \Gamma^i_{22}\boldsymbol{f}^{(2)2} \tag{6.67}$$

is being incorporated into the multidimensional numerical update. The source term on the right hand side of equation (6.56) can be written

$$\boldsymbol{\psi} = \underbrace{\Gamma^i_{11}T^{11} + \Gamma^i_{21}T^{21}}_{x^1 \text{ sweeps}} + \underbrace{\Gamma^i_{12}T^{12} + \Gamma^i_{22}T^{22}}_{x^2 \text{ sweeps}}, \tag{6.68}$$

which is equivalent to (6.67) since $\boldsymbol{f}^{(i)j} = T(\tilde{dx}^{(i)}, \tilde{dx}^{(j)}) = T^{ij}$. This shows that the source term has been absorbed into the flux difference, and therefore into the Riemann problems that are solved at each grid interface.

6.6 Accuracy

The algorithm developed here is intended for applications with discontinuous solutions. It is not expected to achieve a formal order of accuracy greater that one on such solutions. However, second order accuracy in smooth regions of the solution is often important to sharply resolve features away from the discontinuities.

It was demonstrated in Section 3.3 that an algorithm based on f-waves will generate second order numerical solutions if both the spatially-varying flux function, and the solution remain smooth. In the previous section, we found that solving Riemann problems based on fluxes that have been parallel transported is equivalent to incorporating the geometric source term using the modified flux method discussed in Section 4.2. It was also shown that in order to maintain second order accuracy in the presence of a spatially-varying flux, the numerical update for the modified flux method must include the correction (4.45).

The correction (4.45) was written in terms of $\partial\boldsymbol{\psi}/\partial\boldsymbol{q}$ for a general source term $\boldsymbol{\psi}$. For conservation laws on manifolds, the m^{th} component of the source is

$$\psi^{[m]} = \begin{cases} 0 & \text{for scalar components of } \boldsymbol{q} \\ -\Gamma^m_{jk}T^{jk} & \text{for the } m^{\text{th}} \text{ vector component of } \boldsymbol{q}. \end{cases} \tag{6.69}$$

In order to implement the correction (4.45), a vector $\boldsymbol{\mathcal{S}}$ is introduced at each cell edge. Along a slice in the x^1 direction, the m^{th} vector component of $\boldsymbol{\mathcal{S}}^{(1)}_{|i-1/2}$ is defined to be

$$\begin{aligned}
\mathcal{S}^{(1)[m]}_{|i-1/2} &= -\Gamma^m_{jk}\frac{\partial \boldsymbol{f}^{(j)k}}{\partial \boldsymbol{q}}\sum_{p=1}^{n_{eq}}\boldsymbol{\mathcal{Z}}^p_{|i-1/2} \\
&= -\Gamma^m_{1k}\left[A^1_{|i-1/2}\sum_{p=1}^{n_{eq}}\boldsymbol{\mathcal{Z}}^p_{|i-1/2}\right]^{[k]} - \Gamma^m_{2k}\left[A^2_{|i-1/2}\sum_{p=1}^{n_{eq}}\boldsymbol{\mathcal{Z}}^p_{|i-1/2}\right]^{[k]} \qquad (6.70)\\
&= -\Gamma^m_{1k}\left[\sum_{p=1}^{n_{eq}} s^p_{|i-1/2}\boldsymbol{\mathcal{Z}}^p_{|i-1/2}\right]^{[k]} - \Gamma^m_{2k}\left[A^2_{|i-1/2}\left(\boldsymbol{\mathcal{A}}_1^-\boldsymbol{\Delta Q}_{i-1/2} + \boldsymbol{\mathcal{A}}_1^+\boldsymbol{\Delta Q}_{i-1/2}\right)\right]^{[k]},
\end{aligned}$$

where the fact that $\boldsymbol{\mathcal{Z}}^p_{|i-1/2}$ is the p^{th} eigenvector of the approximate Jacobian $A^1_{|i-1/2}$ has been used. The terms in square brackets in the previous equation are vectors with n_{eq} components, but the sum on k only ranges over the spatial dimensions 1 to n_d. To perform the sum, scalar components of these vectors are neglected and only the vector components are included.

The first term on the right side of the last equality in equation (6.70) can be computed using the f-waves and speeds returned by the normal Riemann solvers. The second term involves decomposing the right and left-going fluctuations into eigenvectors of the transverse Jacobian matrix. That is exactly what is done in the transverse Riemann problems described in Section 2.3.2. Therefore, this term can be computed using the transverse fluctuations $\boldsymbol{\mathcal{A}}_2^-\boldsymbol{\mathcal{A}}_1^*\boldsymbol{\Delta q}_{i-1/2}$ and $\boldsymbol{\mathcal{A}}_2^+\boldsymbol{\mathcal{A}}_1^*\boldsymbol{\Delta q}_{i-1/2}$ returned from the transverse Riemann solvers.

These edge vectors can be used to approximate the correction (4.45) as

$$-\frac{\Delta t^2}{2\Delta x^1}\,\frac{1}{2}\left(\boldsymbol{\mathcal{S}}^{(1)}_{|i-1/2} + \boldsymbol{\mathcal{S}}^{(1)}_{|i+1/2}\right). \qquad (6.71)$$

The average is used in the previous correction to approximate the value of $\boldsymbol{\mathcal{S}}^{(1)}$ at the cell center. There is also a correction of this form along the x^2 direction denoted by $\boldsymbol{\mathcal{S}}^{(2)}$.

6.7 Features of the new algorithm

We have now described the details of a new wave propagation algorithm to solve hyperbolic conservation laws of both scalar and vector equations on manifolds. The main features of the algorithm are summarized as follows:

- The spatially-varying flux functions that result from expressing the conservation law on a coordinate basis that covers $\mathscr{M}$ are handled using f-waves.

- The geometrically induced source terms that appear for vector components of $\boldsymbol{q}$ are handled by parallel transporting the components from the cell center to the cell edge prior to solving Riemann problems.

- Corrections needed for a second order method have been shown to require only the data returned by normal and transverse Riemann solvers.

- Riemann problems can be solved in orthonormal frames at the edge of each cell. This allows the use of Riemann solvers based on Cartesian coordinates, as long as the solver returns f-waves.

The unsplit, high-resolution update for conservation laws on manifolds can be written in the form

$$\begin{aligned} \boldsymbol{Q}_{\mathcal{C}}^{n+1} = \boldsymbol{Q}_{\mathcal{C}}^{n} - \frac{\Delta t}{\mathcal{V}_{\mathcal{C}}\, \Delta x^i} \sum_{i=1}^{n_d} \Big[& \boldsymbol{\mathcal{A}}_i^{+} \boldsymbol{\Delta} \tilde{\boldsymbol{Q}}_{\mathcal{C}-} + \boldsymbol{\mathcal{A}}_i^{-} \boldsymbol{\Delta} \tilde{\boldsymbol{Q}}_{\mathcal{C}+} + \tilde{\boldsymbol{F}}_{\mathcal{C}+}^{(i)} - \tilde{\boldsymbol{F}}_{\mathcal{C}-}^{(i)} \\ & + \frac{\Delta t}{4} \left(\boldsymbol{\mathcal{S}}_{\mathcal{C}-}^{(i)} + \boldsymbol{\mathcal{S}}_{\mathcal{C}+}^{(i)} \right) \Big], \end{aligned} \tag{6.72}$$

where the tildes over the fluctuations signify that they are computed based on the modified data $\boldsymbol{f}^{(k)+}_{|i-1/2,j}$ and $\boldsymbol{f}^{(k)-}_{|ij}$. The correction fluxes, $\tilde{\boldsymbol{F}}^{(i)}$, are based on limited f-waves as defined for spatially-varying fluxes in (3.23).

6.8 The scalar field equation

The scalar field equation is useful in describing a number of physical systems for which it is appropriate to test the new algorithm. The equation has the form

$$-\varphi_{,tt} + \vec{\nabla} \cdot \left(\vec{\nabla}\, \varphi \right) = 0, \tag{6.73}$$

where φ is the scalar field. The velocity field for a relativistic perfect fluid with no vorticity and an equation of state $P = \rho$ is the gradient of such a scalar field. An application with a hard relativistic sphere immersed in such a perfect fluid is discussed in Chapter 8. In this chapter the application used is nonrelativistic acoustics. For this application, the second order equation is reduced to a first order system by defining

$$\begin{aligned} p &= \varphi_{,t} \\ \vec{v} &= \vec{\nabla}\, \varphi. \end{aligned} \tag{6.74}$$

In terms of these new variables, equation (6.73) takes the form

$$\begin{aligned} p_{,t} - \vec{\nabla} \cdot \vec{v} &= 0, \\ \vec{v}_{,t} - \vec{\nabla} \cdot \left(p\, \overset{\leftrightarrow}{h} \right) &= 0. \end{aligned} \tag{6.75}$$

If $n_d = 2$, the state vector has the form $\boldsymbol{q} = (p, v^1, v^2)^T$ with one scalar component and two vector components. Since the algorithm developed in this thesis treats all geometric terms within local Riemann problems, it solves equation (6.73) in the form (6.75).

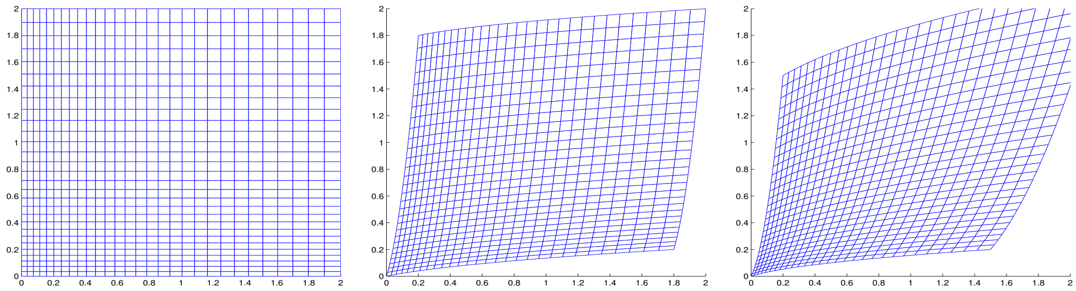

(a) grid-1 (b) grid-2 (c) grid-3

Figure 6.9: Three curvilinear grids with a variety of geometric complexity.

It will be useful to compare solutions generated by the methods discussed here with well established algorithms. To this end, use the covarient invariance of the metric, together with the fact that only stationary metrics are considered to write equations (6.75) in the form

$$\begin{aligned} p_{,t} - v^m_{,m} &= v^m\,\Gamma^j_{mj} \\ v^k_{,t} - h^{km}\,p_{,m} &= 0. \end{aligned} \tag{6.76}$$

In the previous set of equations the definition of the covariant derivative has been used. The standard wave propagation algorithm discussed in Chapter 2 can be applied to the equations in this form. Notice that a generalized Riemann solver must be written to handle the spatially-varying coefficients, h^{km}, that appear in the flux. A split approach can be used to handle the source term in the equation for p.

6.9 A Euclidean manifold: $\mathscr{M} = \mathbb{R}^2$ covered by curvilinear coordinates

The first example considered investigates the behavior of the algorithm on three different curvilinear grids that cover $\mathbb{R}^2$. The grids used in this example are shown in Figure 6.9. These grids are defined by the coordinate transformation

$$\begin{aligned} x \rightarrow x(\xi,\eta) &= \alpha\,\xi + \beta\,\eta + \theta\,\xi^2 + \delta\,\xi\,\eta \\ y \rightarrow y(\xi,\eta) &= \alpha\,\eta + \beta\,\xi + \theta\,\eta^2 + \delta\,\xi\,\eta, \end{aligned}$$

with the parameter values shown in Table 6.2. These grids have been chosen to activate more Christoffel symbols as the grid number increases. By selectively turning Christoffel symbols on, we can test the performance of the method for a wide range of geometric complexity. Figure 6.9 shows the grids defined by parameters in Table 6.2.

The third grid has all nonzero Christoffel symbols. Though the following computation was carried out on all grids, only the results for the third grid are presented. A radially

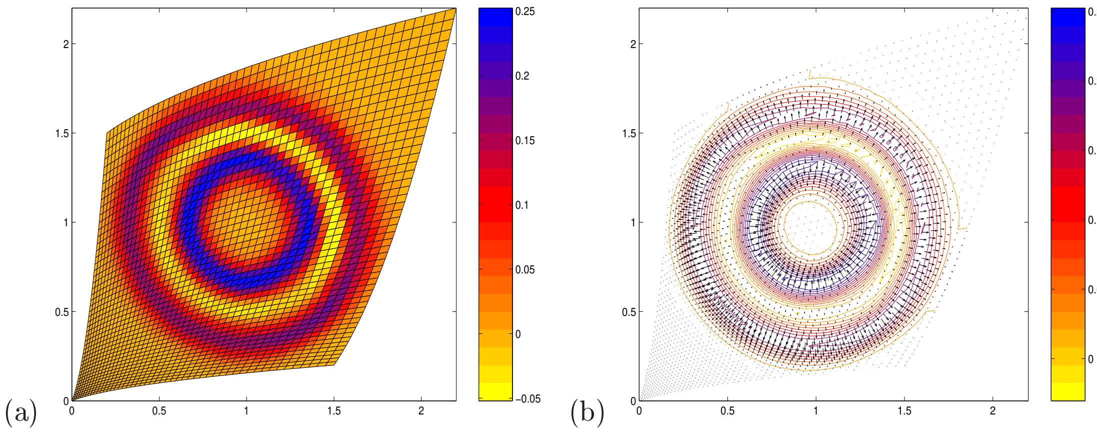

Figure 6.10: (a) A plot of the solution with the physical grid lines. (b) contours of the same solution. Also plotted are vectors indicating the direction of the velocity.

symmetric pressure pulse is initialized on the grid and centered around the point $(x = 1, y = 1)$. The functional form of the pulse is taken to be

$$p(t = 0, r) = \begin{cases} a \cos \frac{\pi |r - r_0|}{\delta} + 1.0) & \text{if } |r - r_0| < \delta \\ 0 & \text{if } |r - r_0| > \delta, \end{cases} \tag{6.77}$$

with no initial velocity. The pressure pulse should split into an in-going and an out-going wave that both remain radially symmetric as they evolve. Using the fact that the solution remains radially symmetric, a highly-resolved one-dimensional computation can be done in the radial direction. This solution can be used to calculate the errors generated by the new algorithm. Figure 6.10(a) shows the solution as it evolves through the physical grid. Notice that the grid lines are skewed, and the volume of the grid cells changes, but the solution remains radially symmetric. Figure 6.10(b) shows the contours of the solution, together with arrows that show the direction of the velocity.

Table 6.2: Parameters used in the curvilinear transformation. The particular parameters are chosen to increase the complexity of the grids. The last grid has all nonzero Christoffel symbols.

	α	β	θ	δ
grid-1	1.0	0.0	1.0	0.0
grid-2	0.5	0.3	1.0	0.0
grid-3	0.5	0.3	1.0	0.5

(a) (b)

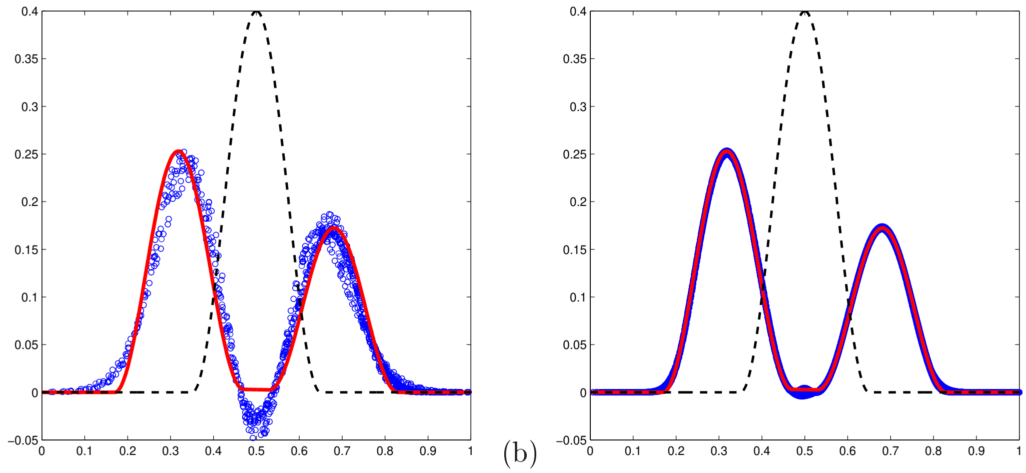

Figure 6.11: (a) A scatter plot of the computed solution on a 50×50 grid. Computed values are displayed as circles, and the solid line represents the highly-refined one-dimensional solution (b) The same as (a) for a 200×200 grid.

The radial symmetry of the solution can be seen in Figures 6.11(a) and 6.11(b). In these figures, the initial condition as a function of r is shown as a dashed line. The solid line represents the highly-refined one-dimensional solution, and the circles represent all the computed points in the grid shown in Figure 6.10(a). Figure 6.11(a) shows the computed solution on a 50×50 grid. Virtually all the scatter is gone on the 200×200 grid shown in Figure 6.11(b). The one-norm errors of the pressure, and both components of velocity for this example are listed in Table 6.3.

6.10 A Riemannian manifold: $\mathscr{M}$ defined by a surface $z = b(x^1, x^2)$

The previous example demonstrates that the algorithm presented in this dissertation can handle nonorthogonal curvilinear coordinates that cover a flat manifold defined by $\mathscr{M} = \mathbb{R}^2$. In this example we compute the solution to equation (6.73) on the Riemannian manifold defined by a surface $z = b(x^1, x^2)$. The examples presented in this section will use the Cartesian coordinates

$$\begin{aligned} x^1 &\to x^1(x, y) = x \\ x^2 &\to x^2(x, y) = y. \end{aligned} \tag{6.78}$$

The surface that defines $\mathscr{M}$ for all the examples in this section is a Gaussian dip with the functional form

$$b(x, y) = \alpha \exp -\frac{\left((x^1 - x_0)^2 + (x^2 - y_0)^2\right)^{1/2}}{\omega^2}. \tag{6.79}$$

Table 6.3: The one norm of the error in the computed pressure, p, first component of the velocity, v^1, and the second component of velocity, v^2.

	Pressure	1-Velocity	2-Velocity
grid	$\Vert p_{\text{exact}} - p_{\text{CLAWMAN}}\Vert_1$	$\Vert p_{\text{exact}} - p_{\text{CLAWMAN}}\Vert_1$	$\Vert p_{\text{exact}} - p_{\text{CLAWMAN}}\Vert_1$
50x50	$.4328 \times 10^{-1}$	$.1328 \times 10^{-1}$	$.1328 \times 10^{-1}$
100x100	$.1364 \times 10^{-1}$	$.4158 \times 10^{-2}$	$.4158 \times 10^{-2}$
200x200	$.3695 \times 10^{-2}$	$.1345 \times 10^{-2}$	$.1345 \times 10^{-2}$
order	1.9	1.6	1.6

The point (x_0, y_0) defines the location in the coordinate plane of the minimum value in the surface. Figures 6.12(a) and 6.12(b) show this surface embedded in a three-dimensional Euclidean space with two different values of the amplitude α.

The Euclidean space in which the surface is embedded has the Cartesian metric

$$[h_{IJ}] = \text{diag}(1, 1, 1), \tag{6.80}$$

where capital Latin indices range over the dimension of the flat Euclidean space, e.g., $I, J \in \{1, 2, 3\}$. Points on the surface are described in this space as $(x, y, b(x, y))$. The metric tensor on the surface can be computed by projecting $[h_{IJ}]$ onto the sub-manifold defined by the surface $b(x, y)$. To do this, define a projection matrix with components $M_I^k = \frac{\partial x^k}{\partial x^I}$ so that the matrix has the form

$$[M_k^I] = \begin{pmatrix} 1 & 0 \\ 0 & 1 \\ b_{,1} & b_{,2} \end{pmatrix}. \tag{6.81}$$

This projection matrix is used to define the metric tensor restricted to the surface by computing

$$\begin{aligned} [h_{kj}] &= \left[M_k^I\right]^T [h_{IJ}] \left[M_j^J\right] \\ &= \begin{pmatrix} 1 & 0 & b_{,1} \\ 0 & 1 & b_{,2} \end{pmatrix} \begin{pmatrix} 1 & 0 & 0 \\ 0 & 1 & 0 \\ 0 & 0 & 1 \end{pmatrix} \begin{pmatrix} 1 & 0 \\ 0 & 1 \\ b_{,1} & b_{,2} \end{pmatrix} \\ &= \begin{pmatrix} 1 + (b_{,1})^2 & b_{,1}\, b_{,2} \\ b_{,1}\, b_{,2} & 1 + (b_{,2})^2 \end{pmatrix}. \end{aligned} \tag{6.82}$$

The fact that the off-diagonal terms of this metric are nonzero implies that the coordinate lines on the surface are skewed. Figure 6.12(b) shows the skewing of coordinate lines that occurs in the region near the dip.

The metric h_{kj} derived above defines the geometry of the two-dimensional manifold on which we solve equation (6.73). One way to get a feel for the geometry defined by h_{kj} is to compute geodesics on the surface. Geodesics are curves that represent the "straightest

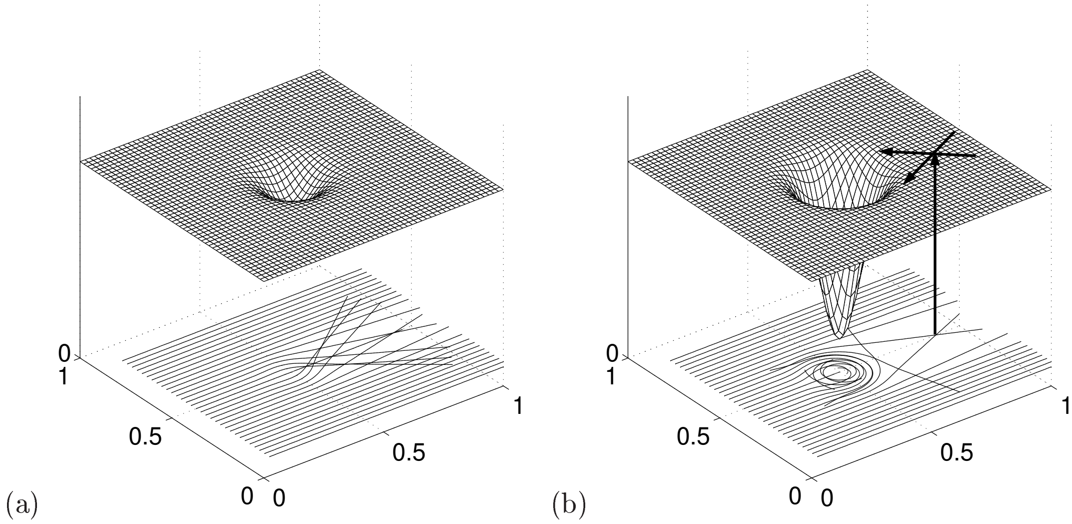

Figure 6.12: The surface that defines $\mathscr{M}$ for the examples presented in Section 6.10. (a) Geodesics initialized as right-going curves along the left boundary are projected down onto a coordinate plane. The depression in the surface causes the geodesics to converge. (b) As the dip gets larger in amplitude, the geodesics converge more and eventually wrap around the center of the surface as shown here.

possible lines" in $\mathscr{M}$. For example, Figure 6.12(a) shows geodesics that are initialized along the left boundary to be right-going. These geodesics are projected down to the coordinate plane for visualization purposes. The figure shows that the geodesics that avoid the dip and travel through the flat space remain straight, but the curves that encounter the dip begin to converge and their paths are altered. If the amplitude of the surface is increased as in Figure 6.12(b), the direction of geodesic curves in $\mathscr{M}$ can be changed entirely.

The geodesics shown in Figures 6.12(a) and 6.12(b) resemble the paths of photons traveling past large clusters of galaxies. Due to Einstein's general theory of relativity, a cluster of galaxies will warp the fabric of spacetime similar to the surface shown in the figures. Clusters with more mass will have larger dips. Light from distant objects will arrive at the cluster traveling in straight and parallel paths much like the geodesics shown in the figures. However, when the light encounters the curvature of the dip produced by the cluster, light rays converge as they do in the figures. Figure 6.12(b) shows the intersection of two light rays that have passed by the dip. An observer at this intersection would see the same object coming from two different directions. This phenomena is called gravitational lensing, and is observed by astronomers.

(a) (b)

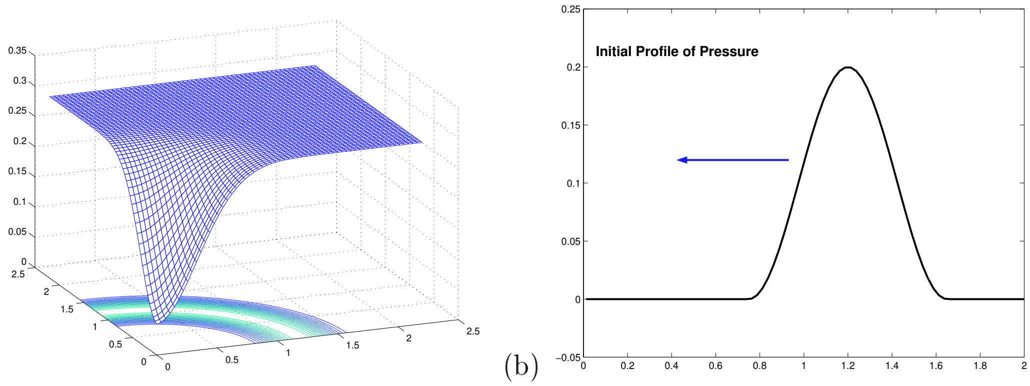

Figure 6.13: (a) The manifold on which the radially symmetric solution is computed. Contours of the initial pressure pulse are shown. (b) The initial profile of the pressure as a function of radius.

6.10.1 Radially symmetric initial conditions

Consider the radially symmetric initial condition (6.77) that was used in Section 6.9. The axis of symmetry is taken to be the location where the surface has its minimum value, (x_0, y_0). Figure 6.13(a) shows the upper quadrant of the surface together with the contours of the initial pressure pulse. Figure 6.13(b) shows the initial condition for the pressure as a function of r. The pulse is initially set up in the flat region outside the surface dip. Once again, the pulse will decay into an out-going and an in-going piece. The out-going pulse will simply radiate away since it only travels in the flat part of $\mathscr{M}$. However, the in-going pulse will interact with the dip in the surface.

Since the initial condition and the surface share the same axis of radial symmetry, the solution will remain radially symmetric. Therefore, a highly-resolved one-dimensional computation can be done by applying the standard wave propagation method to the one-dimensional version of equations 6.76. A split method has been used to handle the source terms. These results can be compared with the results of the new algorithm.

The two-dimensional calculation is done on the upper quadrant shown in Figure 6.13(a). Simple extrapolation boundary conditions are applied to the right and upper boundaries where the manifold is flat. Reflecting boundary conditions are used on the left and lower boundaries. Notice that along boundaries that intersect the dip, grid lines are skewed and the curvature of $\mathscr{M}$ is exponential. These are difficult boundaries to capture.

Figures (6.14(a))-(6.14(d)) show a time evolution of computed data for this radially symmetric pulse. The solid line represents the one-dimensional solution, and the circles represent the solution computed by the new method. All two dimensional data points are shown in the figures. The fact that there is no scatter in the data means that the algorithm maintains the expected symmetry. In Figure 6.14(a), the out-going pulse can be seen leaving the domain at the right edge of the plot. These figures show that the agreement between

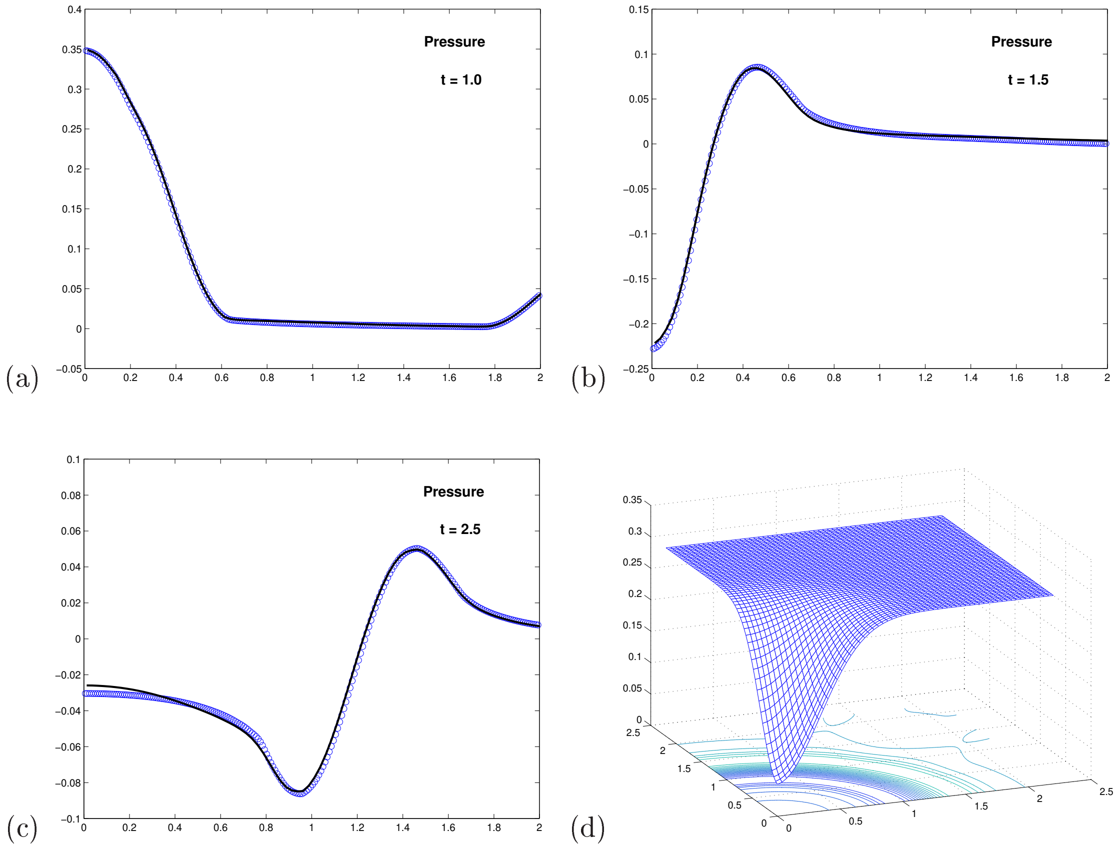

Figure 6.14: The time evolution of the radially symmetric problem. Each image is a scatter plot of all computed data. (a) $t = 1.0$ (b) $t = 1.5$ (c) $t = 2.5$ (d) Contours of the final solution plotted together with the manifold.

the one-dimensional calculation and the new method is good.

6.10.2 Initial conditions with no symmetry

In order to test the multidimensional properties of the new algorithm, initial conditions that share no symmetric axes with the surface dip are used. Specifically, the initial pressure pulse has the functional form

$$p(t=0,x,y) = \begin{cases} a\,\cos\frac{\pi\,(x^1-x_l)}{\delta} + 1.0) & \text{if } |x^1 - x_l| < \delta \\ 0 & \text{if } |x^1 - x_l| > \delta \end{cases}, \tag{6.83}$$

where x_l is taken to be a value in the flat region near the left edge of the grid. This pulse is initialized to be right-propagating. As the wave travels to the right, part of it interacts with the dip in the surface as shown in Figures (6.15(a))-(6.15(f)). In these figures, the

Table 6.4: The one-norm values of the difference between pressures and velocities computed by CLAWMANand CLAWPACKas the grid is refined.

	Pressure	1-Velocity	2-Velocity
Cells	$\Vert p_{\text{CLAWPACK}} - p_{\text{CLAWMAN}}\Vert_1$	$\Vert v^1_{\text{CLAWPACK}} - v^1_{\text{CLAWMAN}}\Vert_1$	$\Vert v^2_{\text{CLAWPACK}} - v^2_{\text{CLAWMAN}}\Vert_1$
50	$.361 \times 10^{-4}$	$.236 \times 10^{-4}$	$.173 \times 10^{-4}$
100	$.192 \times 10^{-4}$	$.103 \times 10^{-4}$	$.110 \times 10^{-4}$
200	$.511 \times 10^{-5}$	$.313 \times 10^{-5}$	$.332 \times 10^{-5}$
order	1.9	1.7	1.7

surface is plotted together with the projection of the pressure onto the coordinate plane. They show the time evolution of the pulse as it interacts with the geometry of the dip. The solution that is shown in these figures can be understood by looking at the geodesics of Figure 6.12(b). Two effects that the geometry have on geodesic curves are demonstrated in that figure. First, curves that interact with the edge of the dip converge and cross on the down-wind side of the dip. Second, curves that interact with the central region of the dip can end up heading in the same direction that they came from. Both of these effects are seen in Figures (6.15(a))-(6.15(f)). In Figure 6.15(c) it appears that the pressure wave is following the geodesics of the surface. In the figures that follow, a small pressure wave begins to travel in the direction from which it came. Notice that the portion of the wave that does not interact with the geometry continues on as it would in a Cartesian space.

This solution can be compared to a numerical solution computed by the standard wave propagation algorithm. In order to apply the standard methods to this problem, equation (6.73) needs to be cast in the form (6.76). Specifically, on this surface these equations take the form

$$
\begin{aligned}
p_{,t} - (v^1)_{,1} - (v^2)_{,2} &= \left(\frac{b_{,1}b_{,11} + b_{,2}b_{,12}}{1 + (b_{,1})^2 + (b_{,2})^2}\right) v^1 + \left(\frac{b_{,2}b_{,22} + b_{,1}b_{,12}}{1 + (b_{,1})^2 + (b_{,2})^2}\right) v^2 \\
v^1_{,t} - \left(\frac{1 + (b_{,2})^2}{1 + (b_{,1})^2 + (b_{,2})^2}\right) p_{,1} &+ \left(\frac{b_{,1}b_{,2}}{1 + (b_{,1})^2 + (b_{,2})^2}\right) p_{,2} = 0 \\
v^2_{,t} + \left(\frac{b_{,1}b_{,2}}{1 + (b_{,1})^2 + (b_{,2})^2}\right) p_{,1} &- \left(\frac{1 + (b_{,1})^2}{1 + (b_{,1})^2 + (b_{,2})^2}\right) p_{,2} = 0.
\end{aligned}
\tag{6.84}
$$

A Riemann solver that can handle the spatially-varying functions that appear in the flux for the velocity must be used together with a split method to handle the source term in the pressure equation. Figures (6.16(a))-(6.16(f)) show a comparison between the pressures and velocities computed by the standard wave propagation method, and the new algorithm developed in this thesis. Small oscillations that appear in the contours of the solution generated by CLAWMAN are an artifact of setting the contour levels by the maximum and minimum values of the solutions generated by CLAWPACK. These figures show that the two methods generate the same solution.

This is a significant test of the new algorithm for the following reasons:

1. The solutions being compared in Figures (6.16(a))-(6.16(f)) were generated by solving different forms of equation (6.73). The solution generated by CLAWMAN came from the system in the form (6.75), and the solution generated by CLAWPACK came from the system in the form (6.76).

2. Geometric terms that appear in both forms of the equations are handled by each method using entirely different techniques.

3. The CLAWPACK software is extensively used for many different applications. It has been shown to generate accurate and robust solutions.

The agreement of these numerical solutions is demonstrated in Table 6.4. The one-norm difference of the computed solutions on various grids is shown in this table. As the grid is refined, the solutions generated by the two methods converge.

The advantages of using the new algorithm include:

1. Using f-waves locally incorporates the changing volume of grid cells into Riemann problems. The standard algorithm is forced to treat the changing volume with a source term.

2. Using parallel transport locally incorporates the geometrically induced source that appears in the equations for the velocity components.

3. The Cartesian version of the Riemann solver can be used. For complicated systems like relativistic magneto-hydrodynamics, this will likely be a necessary feature.

In the next chapter we discuss an implementation of the new algorithm in the software package CLAWMAN that was used to generate the examples in this chapter.

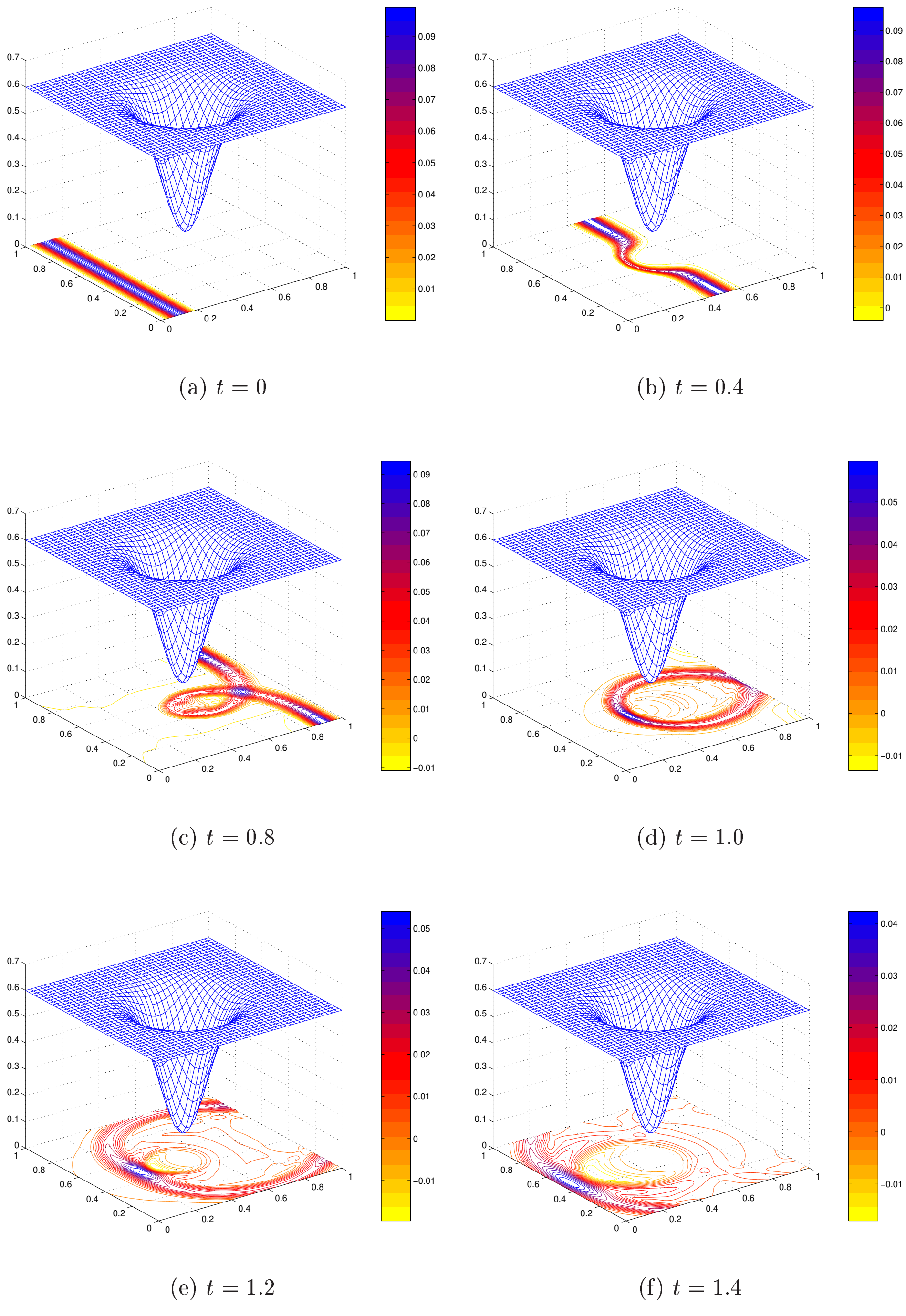

(a) $t = 0$

(b) $t = 0.4$

(c) $t = 0.8$

(d) $t = 1.0$

(e) $t = 1.2$

(f) $t = 1.4$

Figure 6.15: A time sequence of the multidimensional solution. The contours of the solution are plotted on a plane projected down from the manifold.

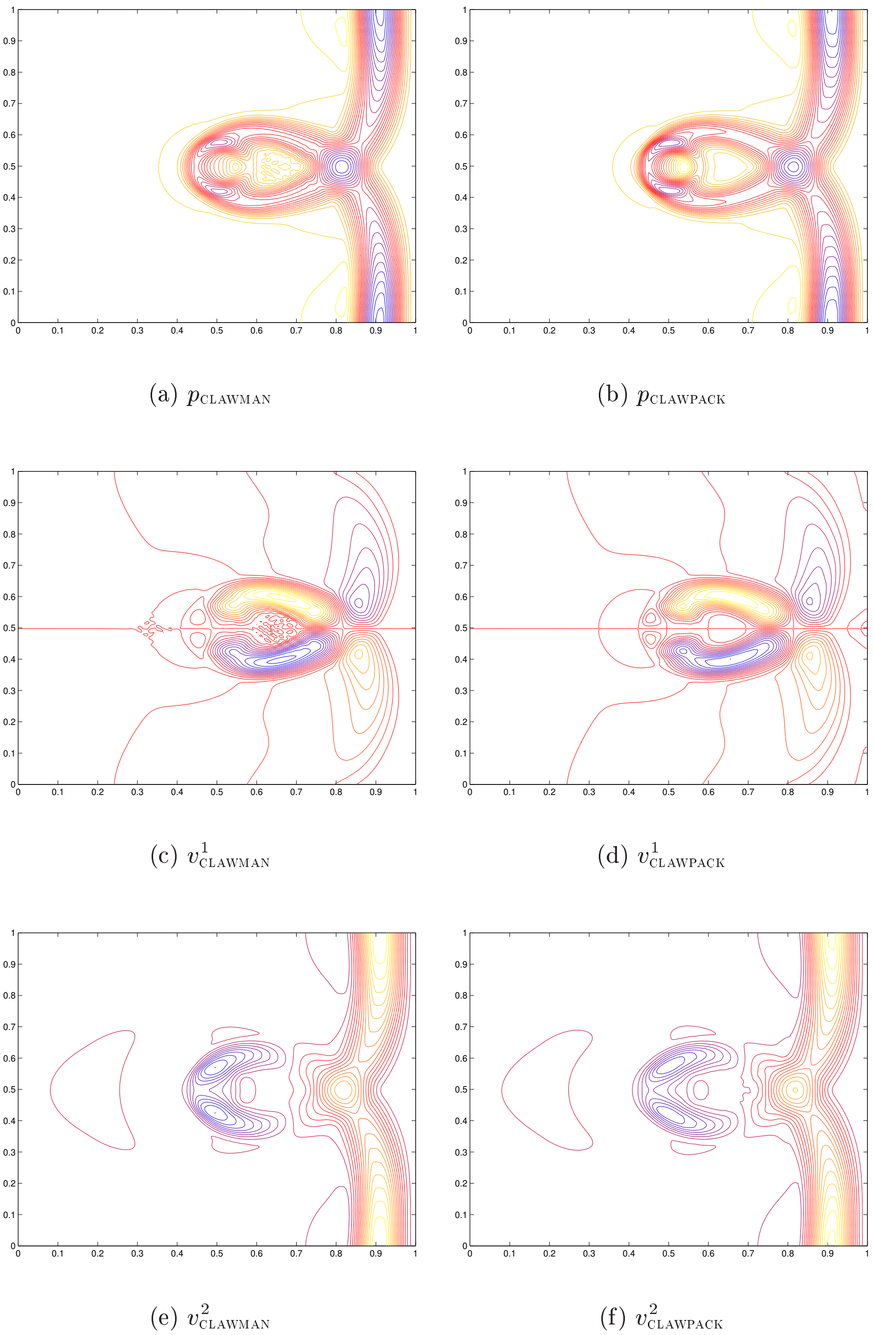

(a) p_{CLAWMAN} (b) p_{CLAWPACK}

(c) v^1_{CLAWMAN} (d) v^1_{CLAWPACK}

(e) v^2_{CLAWMAN} (f) v^2_{CLAWPACK}

Figure 6.16: A comparison of the pressure and velocity computed by CLAWMAN and CLAWPACK for the multidimensional example.